

THE INFRARED SPECTRUM OF METHYL CHLORIDE IN THE 1.8 MICRON REGION

Thesis for the Degree of M. S.
MICHIGAN STATE UNIVERSITY
Robert G. Brown
1957

THE INFRARED SPECTRUM OF METHYL CHLORIDE IN THE 1.6 MICRON REGION

ру

Robert G. Brown

A THESIS

Submitted to the College of Science and Arts Michigan State University of Agriculture and Applied Science in partial fulfillment of the requirements for the degree of

MASTER OF SCIENCE

Department of Physics and Astronomy
1957

To

C. F. B.

and

M. K. B.

ACKNOWLEDGEMENTS

The author wishes to express his thanks to Dr. T. H. Edwards for suggesting the problem, and for the guidance and assistance extended throughout the work. He also wishes to express appreciation for the financial support of the Research Corporation during the academic year 1955-56.



THE INFRARED SPECTRUM OF METHYL CHLORIDE IN THE 1.6 MICRON REGION

рд

Robert G. Brown

AN ABSTRACT

Submitted to the College of Science and Arts Michigan State University of Agriculture and Applied Science in partial fulfillment of the requirements for the degree of

MASTER OF SCIENCE

Department of Physics and Astronomy
1957

Approved Medwards

Robert G. Brown

ABSTRACT

Using a high resolution plane grating vacuum spectrometer, the infrared absorption spectrum of the symmetric top molecule methyl chloride was examined in the region near 6000 cm⁻¹. Spectral calibration was achieved by utilizing Edser-Butler bands from a Fabry-Perot etalon to interpolate between Argon emission lines as frequency standards.

The rotational fine structure of the parallel component of the overtone band $2\frac{1}{4}$ was resolved. Q branches for K = 2 to K = 10 were identified, as were P and R branch lines belonging to the K = 3 sub-band. Analysis yielded the following values (in cm⁻¹) for the molecular constants:

band origin $V_0 = 6015.56$ (A'-B')-(A''-B'') = -0.0481 B' = 0.4439 B'' = 0.4436B''-B'' = 0.00044

where $A = h/8\pi^2 cI_A$, $B = h/8\pi^2 cI_B$, I_A is the moment of inertia about the unique principal axis, I_B is the moment of inertia about one of the two equivalent principal axes, and the single and double prime refer to the upper vibrational state and to the ground state respectively.

TABLE OF CONTENTS

Introduction	1
Spectrometer	
Optical Paths	3
Alignment of Interferometer System	7
Monochromator	9
Alignment of Monochromator	13
Curvature of Image	22
Width of Image	24
Grating Ghosts	28
Amplifiers and Recorder	29
Absorption Cell	30
Light Sources	30
Symmetric Top Theory	31
Vibration-Rotation Energy	33
Transition Energies	38
Sub-Bands	39
Intensity Alternation	40
Isotope Effect	42
Spectra and Analysis	44
Wavelength Standards	44
Q Branches	4 6
Identification of K = 3 Sub-Band	50
P and R Branch Analysis	52
Summary of Results	55
Perturbation	65
Note on Isotope Effect	66
Bibliography	68

LIST OF TABLES

Tabl e		Page
I.	Variation of Image Width with Grating Position	26
II.	Vibrational Modes in CH3Cl	33
III.	Standard Argon Emission Lines	46
IV.	Q Branch Frequencies	48
٧.	Summary of Constants	58
VI.	P Branch Frequencies	61
VII.	R Branch Frequencies	63

LIST OF FIGURES

Figure		Page
1.	Spectrometer	4
2.	Spectrometer (photograph)	5
3.	Foreoptics for infrared beam	6
4.	Foreoptics for calibration beam	6
5.	Monochromator	10
6.	Grating surface	11
7.	Grating mount	12
8.	Displacement of grating during rotation	12
9.	Position of flat for adjustment of paraboloid	14
10.	Arrangement for lateral adjustment of paraboloid	15
11.	Arrangement for focussing paraboloid	15
12.	Paraboloidal mirror mount	16
13.	Variation of image position with rotation of grating	18
14.	Grating mount	19
15.	Position of source point with respect to tilted grating	20
16.	Variation of image width with grating position	27
17.	Methyl chloride molecule	31
18.	Normal vibrations of CH3Cl	32
19.	Sub-bands	41
20.	Parallel component of $2\mathcal{V}_{\scriptscriptstyle A}$	45

Pigure	•	Page
21.	Q branches	47
22.	Graphical analysis of Q branches	4 9
23.	Line structure	51
24.	$R(\tilde{z}-1) + P(J) \text{ vs. } J^2$	54
25.	R(J) - P(J) vs. J	56
26.	R(J-1) - P(J+1) vs. J	57 ⁻
27.	Effect of perturbation on line position	65

.

INTRODUCTION

Among reports on the methyl halides, there is no report of high resolution work on methyl chloride in the lead sulfide region, i.e. approximately 1 micron to 2.7 microns. This region was examined under high resolution, and several strong absorption bands were found. Near 6000 cm⁻¹, there were observed a parallel and a perpendicular band attributed to $2\mathcal{V}_4$, and at least one other band of complex perpendicular structure. This work was directed at the absorption assigned to $2\mathcal{V}_4$.

Spectra were obtained using a self-recording vacuum spectrometer with a plane grating in the Pfund-type monochromator and lead sulfide detection. Spectral calibration was achieved by using the Edser-Butler bands of constant frequency difference produced by a Fabry-Perot etalon, in conjunction with the monochromator, to interpolate between standard argon emission lines. Both infrared and calibration signals were recorded simultaneously on a single chart by a Leeds & Northrup two pen recorder.

Under high resolution, the perpendicular component of 2 24 exhibits anomolies which indicate the presence of a perturbation. Consequently, it has not yet been possible to determine the origin for this component. It was possible, however, to analyze the rotational fine structure of the parallel band. Q branches for K = 2 to K = 10 were identified and analyzed. Apparently for the first time, P and R

branch lines in a single sub-band were identified. Pickworth and Thompson (22) have performed analyses on composite lines in the \mathcal{L}_1 and 2 \mathcal{L}_5 bands of methyl chloride and, from their results, estimated a value of K corresponding to the intensity maxima in the P and R branches. From their results, Wiggins, Shull, and Rank (23) have calculated the line structure for the 2 \mathcal{L}_4 band of methyl bromide to match the observed envelope of the P and R branch lines and showed that the intensity maxima corresponded to a particular K value.

In this work, the K = 3 sub-band was identified, and the P and R branch analysis was then performed on lines in this sub-band. Results obtained are generally satisfactory.

Problems requiring further work are an apparent perturbation near J = 20 in the parallel band, and the analysis of the perpendicular component of $2 \mathcal{V}_4$. To complete work in this region for the present, the complex perpendicular structure near $2 \mathcal{V}_4$ should be analyzed.

SPECTROMETER

The spectrometer employed is a plane grating, vacuum instrument designed and built by R. H. Noble (1) and described elsewhere by Nichols (2). Recently, alterations and additions have been made. Most notable among these changes are new gratings and a system to provide interferometric fringes for calibration. The present system is illustrated in Figures 1 and 2.

Optical Paths

Introduction of an interforometer system for calibration purposes necessitated modifications which permit dual optical paths. The infrared beam and the beam of visible light for calibration traverse separate paths until they enter the monochromator wherein their paths involve the same optical elements. Upon emerging from the monochromator, the beams follow separate paths to the detectors. The elements of the two systems are illustrated separately in Figures 3 and 4.

The infrared beam enters the spectrometer through the slit S_1 (Figure 3) and is deflected to the spherical mirror M_1 by the plane mirror F. M_1 focuses the tangential (here vertical) stigmatic image at the entrance slit to the monochromator S_2 . Prior to entry into the monochromator, the

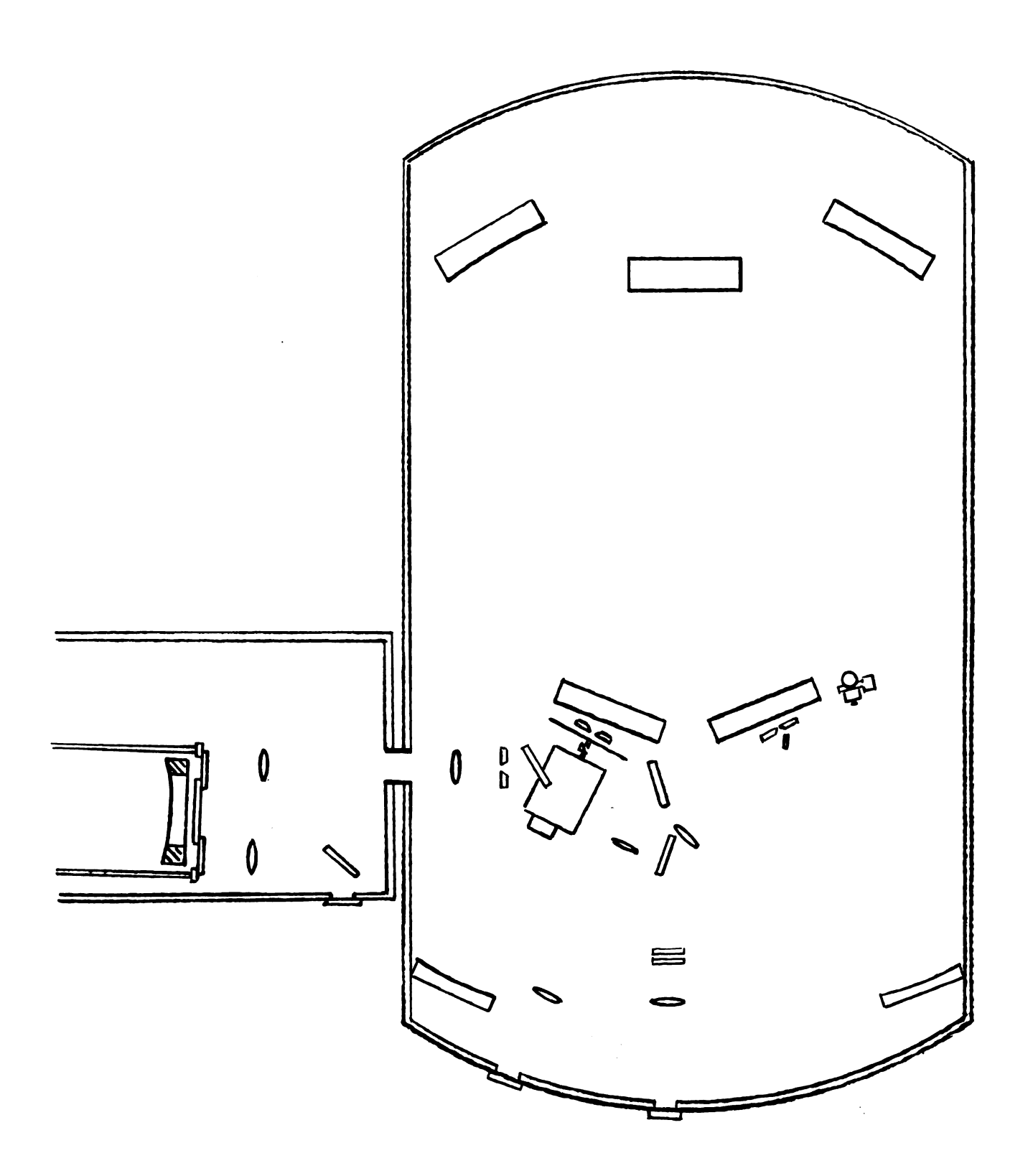
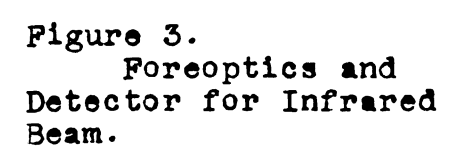
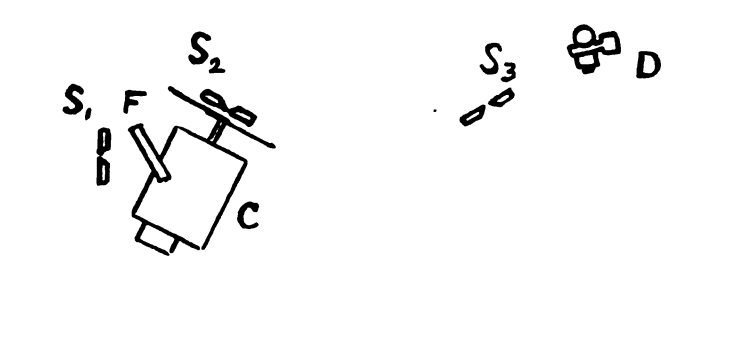


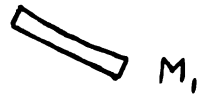
Figure 1. Spectrometer. Multiple traverse cell is shown in position in auxillary tank at left.

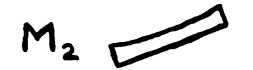
Figure 2. Spectrometer

beam is chopped at 450 cps by the chopper C. The beam emerges from the monochromator at the slit S_3 and is incident upon the spherical mirror M_2 . Again, the tangential image is utilized, this time being focussed upon the Eastman-Kodak Ektron lead sulfide photoconducting cell at D. Two









lead sulfide cells were used, an older 5 mm x 1 mm cell and a newer 0.2 mm x 2 mm cell. The latter was used to obtain the records which were measured.

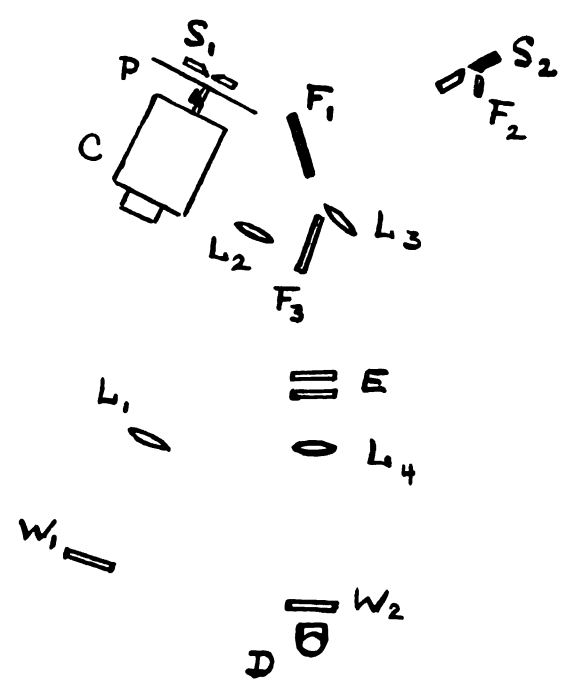


Figure 4.
Optical
System and
Detector for
Visible Calibration Beam.

Outside the monochromator, the visible beam traverses a path through the optical elements drawn in Figure 4. The beam enters the evacuated tank at the quartz window W, and is approximately collimated by the lens L_1 . Lens L_2 produces a converging beam which is focussed at the entrance slit following reflections at the plane mirror F_1 and the aluminized prism P. This prism is located just above the shaft which carries the chopper blade, and reflects the beam into the monochromator below the infrared beam. Since there are an odd number of reflecting surfaces in the monochromator, the visible beam emerges above the infrared beam. Plane mirrors F_2 and F_3 deflect the beam to a collimating lens L_3 . collimated beam passes through a Fabry-Perot etalon E, and is focussed by lens L4 upon the photomultiplier D which is situated outside the tank, together with a filter and the necessary electronic apparatus.

Alignment of Interferometer System

The interferometer system was aligned as follows. With mirrors F_2 and F_3 (Figure 4) and lens L_3 in approximate position, a telescope was mounted outside the spectrometer with its axis in the horizontal plane containing the center of the window W_2 in the end of the tank. Mirrors F_2 and F_3 were then adjusted until the beam emerged through the center of the window W_2 . Still employing the telescope, focussed at infinity,

lens L_3 was moved until it produced a collimated beam. With the telescope removed, lens L_4 was inserted in such a position to form an image at the detector, and, with the photomultiplier removed, a microscope was so positioned that the image of the exit slit was centered in the field. The interferometer was then introduced. A high pressure mercury arc was substituted for the continuous source, and the grating was rotated until the light of the green line traversed the interferometer.

For an extended source, such an optical system would produce an interferometer pattern of concentric rings. In this case, however, the source is very small; it is the illuminated portion of the exit slit. Consequently, only a very small portion of the complete pattern, a narrow strip, is observable. Furthermore, the intensity of the fringe system is low, for the beam has been dispersed by the monochromator. With only a narrow section of the ring system to observe, it is extremely difficult to identify the center of the pattern. With the introduction of an auxillary source, however, a complete pattern becomes visible and adjustment of the interferometer is greatly facilitated.

A sodium lamp was placed on the spectrometer bed near the exit slit of the monochromator without intercepting the beam entering the interferometer system from the exit slit. Enough sodium light, scattered and/or reflected from elements near the exit slit, entered the interferometer so that one could observe a complete fringe system superimposed on the fractional mercury

green line pattern which had its source at the exit slit. With this arrangement, the position of the interferometer was adjusted until the fringe systems were centered in the field of the microscope.

To obtain maximum intensity variation, energy incident upon the photomultiplier was limited to a portion of the central spot of the fringe system. This was done by constructing with an opaque tape an aperture on the window of the tank. To establish the size and position of this aperture, the pattern was observed through the microscope while the tape was being placed on the window.

For the particular region in which work was done, the fringe system was formed from the third order spectrum of visible light. To eliminate overlapping orders, an appropriate filter was placed in the light path ahead of the photomultiplier.

Monochromator

The monochromator is a Pfund type optical system, which incorporates on-axis paraboloidal mirros and pierced flats. During operation, the grating is rotated; its position determining the portion of the spectrum received by the detector. All other components of the monochromator are stationary while spectra are being recorded.

Bilateral entrance and exit slits are located at the foci of the paraboloids. Thus, light entering the system through the entrance slit S_1 (Figure 5) is rendered plane by

the paraboloid P_1 , and is then directed to the grating G by the pierced flat F_1 . That part of the spectrum which will be observed must be incident upon the second flat F_2 at such an angle that, following reflection, the beam has the direction of the axis of the paraboloid P_2 . This part of the

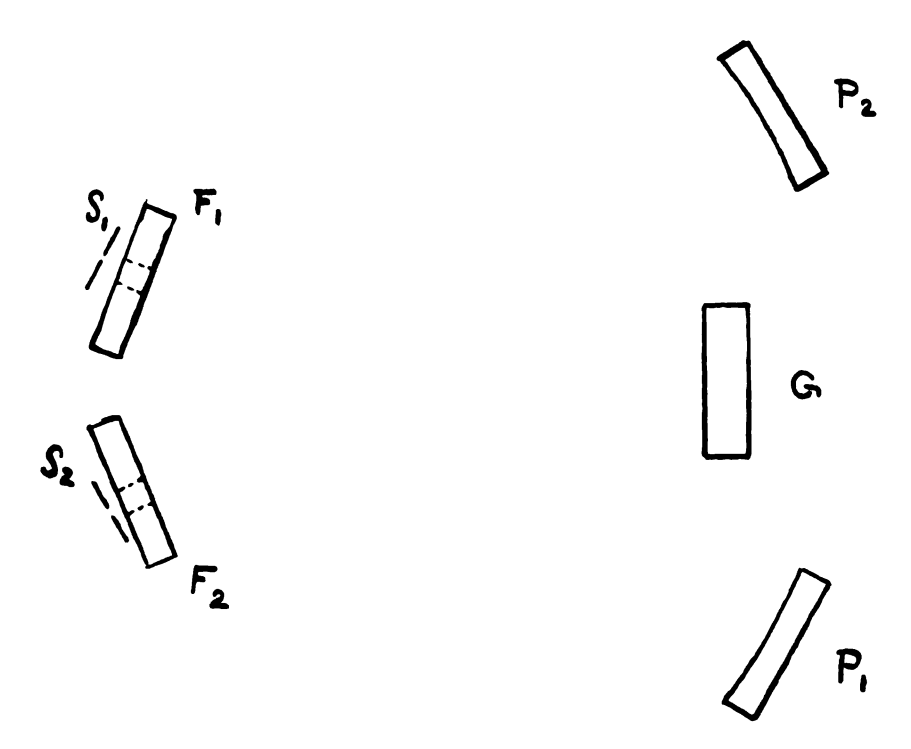


Figure 5. Monochromator

diffracted beam, still composed of parallel light is subsequently focussed on the exit slit. Rotation of the grating sweeps the spectrum across the exit slit.

The two gratings employed are Bausch and Lomb plane echelette replica gratings. One is ruled with 600 lines/mm and is blazed at 27 degrees (Figure 6). Like other blazed gratings, it is doubly blazed, so there are directions on each side of the normal in which energy is concentrated, i.e. in those directions determined by the action of the surfaces

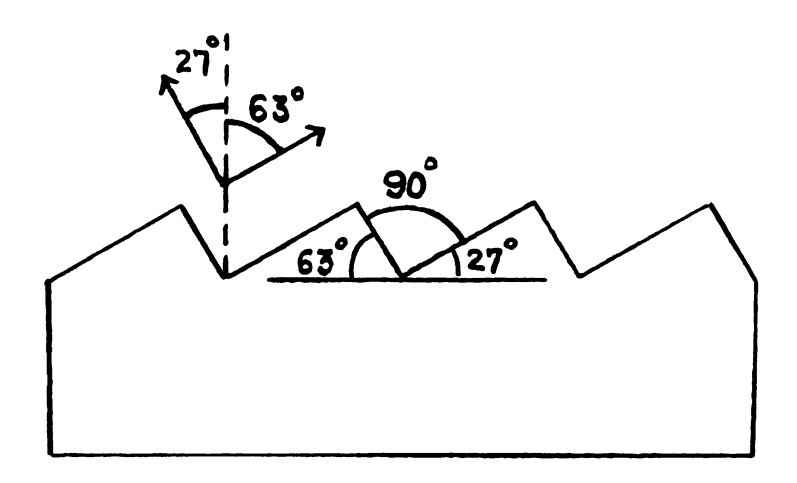


Figure 6. Grating Surface

of the blaze as plane mirrors. Though the angle of the second blaze was not determined, it is probably about 63 degrees, assuming the customary 90 degree diamond ruling tip. For this reason, it may be advantageous to examine different regions of the spectrum on different sides of the central image. Specifically, when investigating regions at angles smaller than about 45 degrees, it is usually best to work on the 27 degree blaze side of the central image. Conversely, those regions of the spectrum occurring at larger angles are enhanced by the 63 degree blaze and are examined on that side of the central image.

The second, and newer, grating is ruled with 400 lines/mm and is blazed at 37 degrees. To take advantage of the blaze, it was necessary to work in second order when using this grating. The spectral records ultimately measured were obtained with this grating.

As a consequence of the particular grating mount, rotation of the grating in both directions from central image position introduces a complication. The grating mount is such that the plane of the diffracting surface is about 7 cm in front of the axis of rotation (Figure 7). Upon rotation

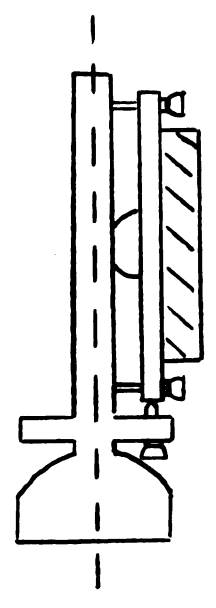


Figure 7.
Grating mount
from side, showing
axis of rotation
(dotted line).

to desired angles, then, the grating suffers significant displacement (Figure 8). It is thus necessary to adjust the

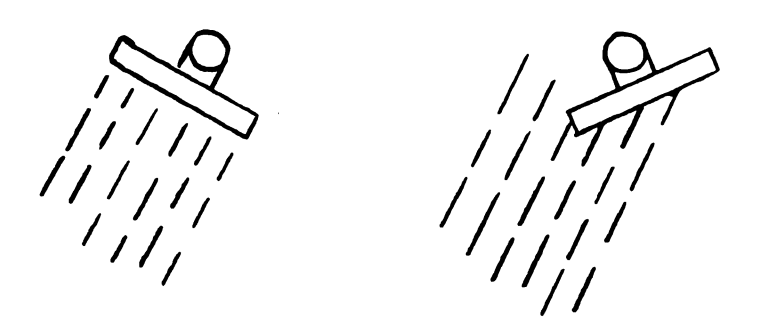


Figure 8. Schematic diagram of two grating positions with fixed direction of incident light beam.

flats in order that the incident light beam be centered on the grating in a particular region of usage. The mounting has a compensating advantage, however, in that two gratings may be simultaneously mounted and aligned. Since considerable time and auxillary apparatus are required to align a grating correctly, and since it is sometimes desirable to employ different gratings, it is a convenience to have alternative gratings ready for immediate us. Furthermore, the two gratings may be interchanged without removing them and exposing the delicate diffracting surfaces to injury.

Alignment of Monochromator

The first step in the alignment of the monochromator is to so adjust the paraboloids that the entrance and exit slits are at the foci of the paraboloids diagonally opposite. In order to bring about this condition, each slit, companion flat, and the paraboloid diagonally opposite were first adjusted as a unit (Figure 9).

with the paraboloid in approximate position and the flat as nearly as possible normal to the axis thereof and centered, the slit was illuminated and the image focussed on the slit. A long, thin plane piece of material was then inserted vertically into the beam (Figure 10). The flat and paraboloid were then adjusted until the shadows on the slit and associated flat, and along the diameter of the paraboloid were of

minimum width. When this situation was achieved, the slit was in a plane containing the axis of the paraboloid.

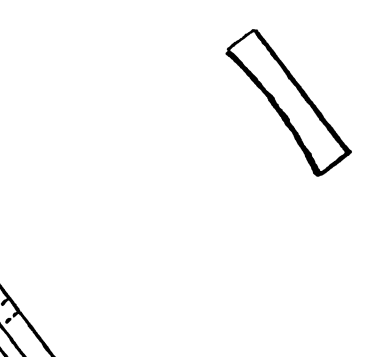


Figure 9. Position of flat for adjustment of paraboloid.

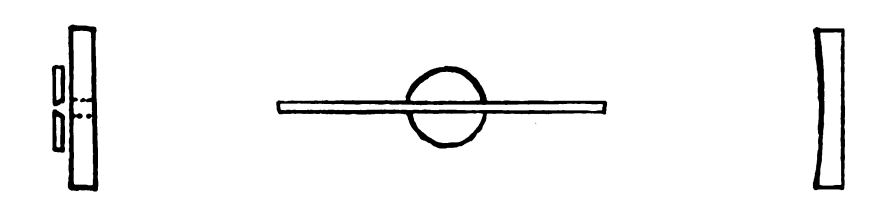


Figure 10. Arrangement for lateral adjustment of paraboloid.

To focus the paraboloid, the arrangement illustrated in Figure 11 was employed. A source S of low intensity (6 Volt pilot bulb) was selected in order that the image could be Viewed directly without discomfort. With the lens L and



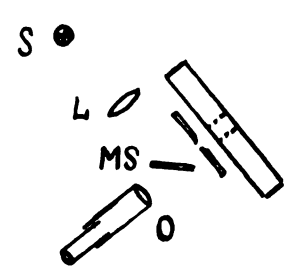


Figure 11. Arrangement for focussing paraboloid.

microscope slide MS, light was focussed upon the slit at the same height above the spectrometer bed as the center of the paraboloids. A microscope slide was chosen in order that the image could be examined when returned to the center of the slit. Utilizing a 30% microscope at 0 to determine the plane of focus, the paraboloid, screw-driven in a dovetailed slide (Figure 12), was moved along its axis until the image was in focus at the slit.

With only the microscope removed from the preceding arrangement, the surface of the paraboloid was viewed with the naked eye through the microscope slide and at the center of the slit. The pierced flat was rotated about a horizontal

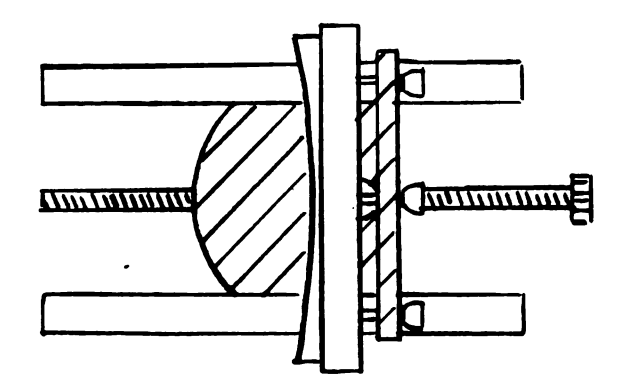


Figure 12. Paraboloidal mirror mount.

axis until dust particles on the surface of the paraboloid were in coincidence with their own shadows returned from the flat. Under this condition, light incident upon the flat is reflected back along the path of incidence. The paraboloid was tilted to bring the image to the chosen center of the slit, and the image refocussed on the slit using the microscope as detailed above.

The next step is to integrate, via the grating, each slit and mirror unit into the system as a whole. To do so, the flat and its mount were rotated until the beam was incident upon the grating. With the grating driven to such a position that the central image was returned to the same

slit, the flat was rotated about a horizontal axis until the image was formed at the position of the signal.

When this procedure was completed for each slit and mirror unit, and the monochromator used in the normal manner, a signal introduced at the chosen "center" of the entrance slit should have emerged at the same height above the spectrometer bed at the exit slit. It was found, however, that the vertical position of the image at the exit slit varied greatly with rotation of the grating. Specifically, with the signal at a fixed position at the entrance slit, the image appeared increasingly lower as the grating was rotated in either direction from central image position (Curve I, Pigure 13). Ease of detection and simultaneous use of the monochromator for two separate beams require that the image emerge from the monochromator at a fixed position on the exit slit. Vertical wandering of the image indicated that the grating was not properly aligned with respect to the rest of the system.

In general, there are three possible errors in grating alignment, any or all of which may be present. In the first place, the plane of the diffracting surface may not be parallel to the axis of rotation. Furthermore, even if the diffracting surface is parallel to the axis of rotation, the rulings may not be parallel to it. The grating mount incorporates means of correcting both of these situations (Figure 14). Finally, the axis of rotation may not be parallel to the plane of the monochromator as defined by the axes of the paraboloids which

: •• •

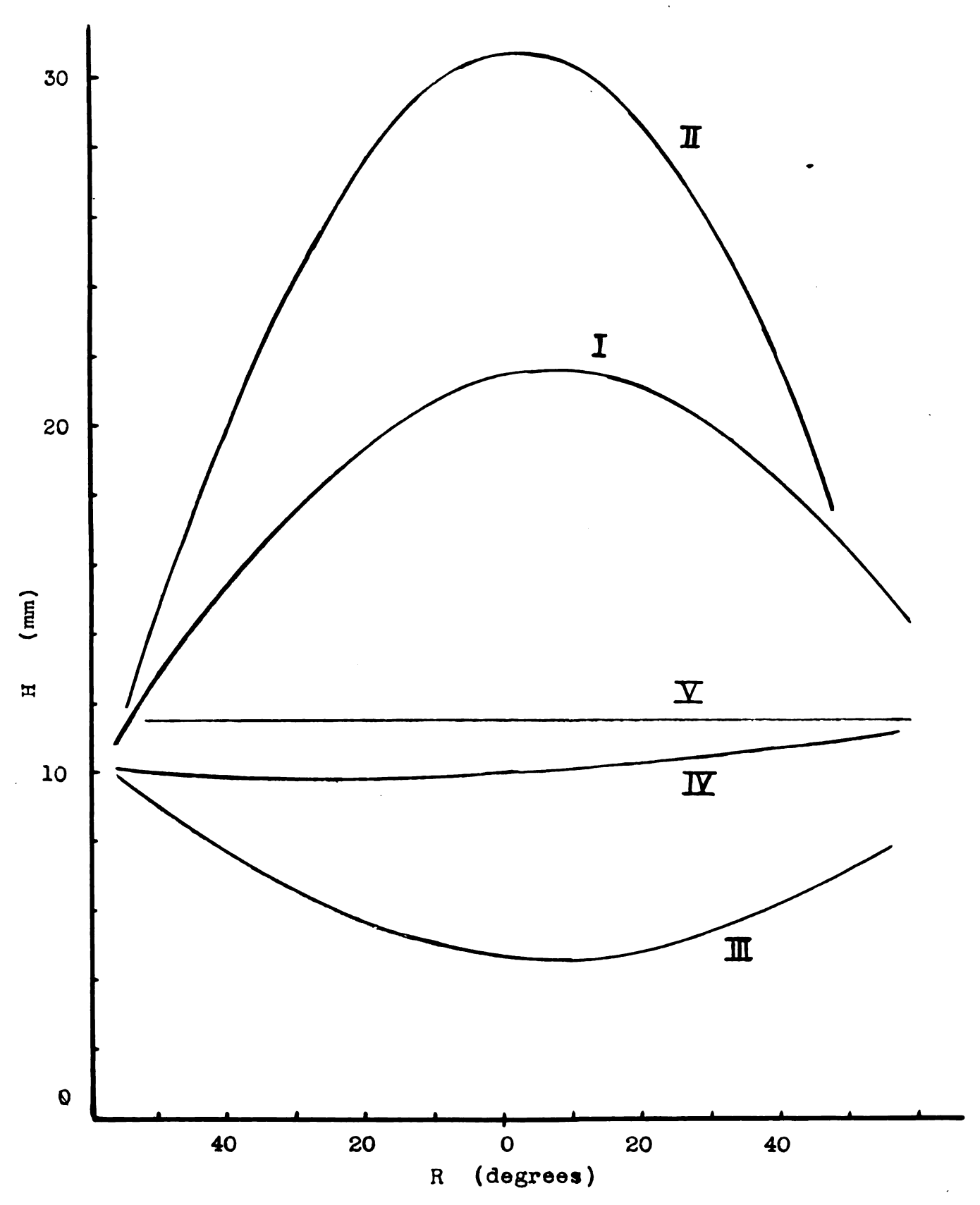


Figure 13. Height H of image above spectrometer bed vs. rotation R of grating from central image position. Zero is arbitrary.

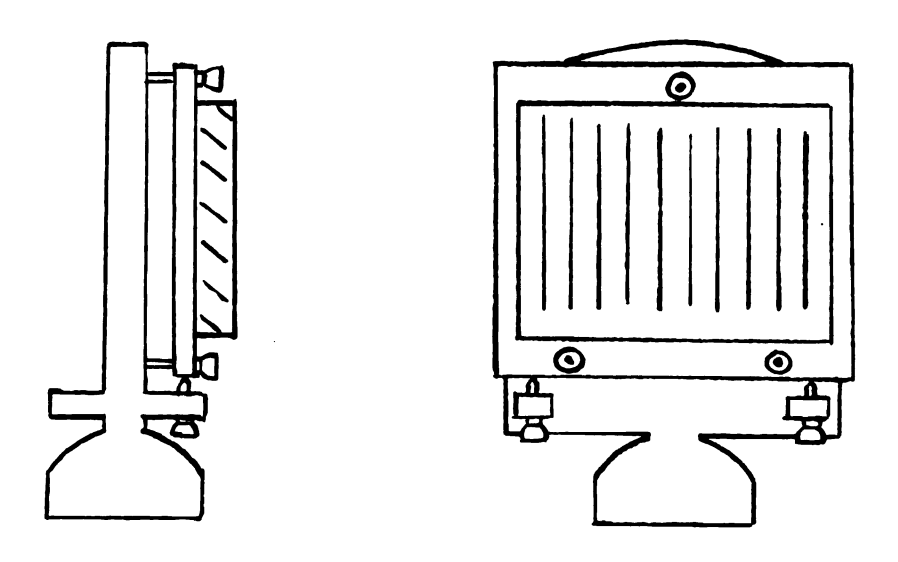


Figure 14. Grating mount.

were adjusted to be parallel to the spectrometer bed. However, the axle which drives the grating is fixed in the spectrometer bed. If the axle is exactly normal to the spectrometer bed, the plane of the monochromator is also defined by the axis of rotation. If the axle is not perpendicular to the spectrometer bed, then the axis of rotation must be used to determine the plane of the monochromator, and the axes of the paraboloids must be adjusted to lie in the plane so defined.

Each of the preceding errors has a unique effect upon the position or formation of the image. The consequences of the errors may be seen by considering each individually while assuming that alignment is otherwise correct. If the grating is tilted with respect to the axis of rotation, the image is displaced from its former position in a manner depending upon the degree of tilt and upon the angles of incidence and diffraction. Let r be the distance from the grating to a point 0 at the entrance slit (Figure 15). The point 0 lies

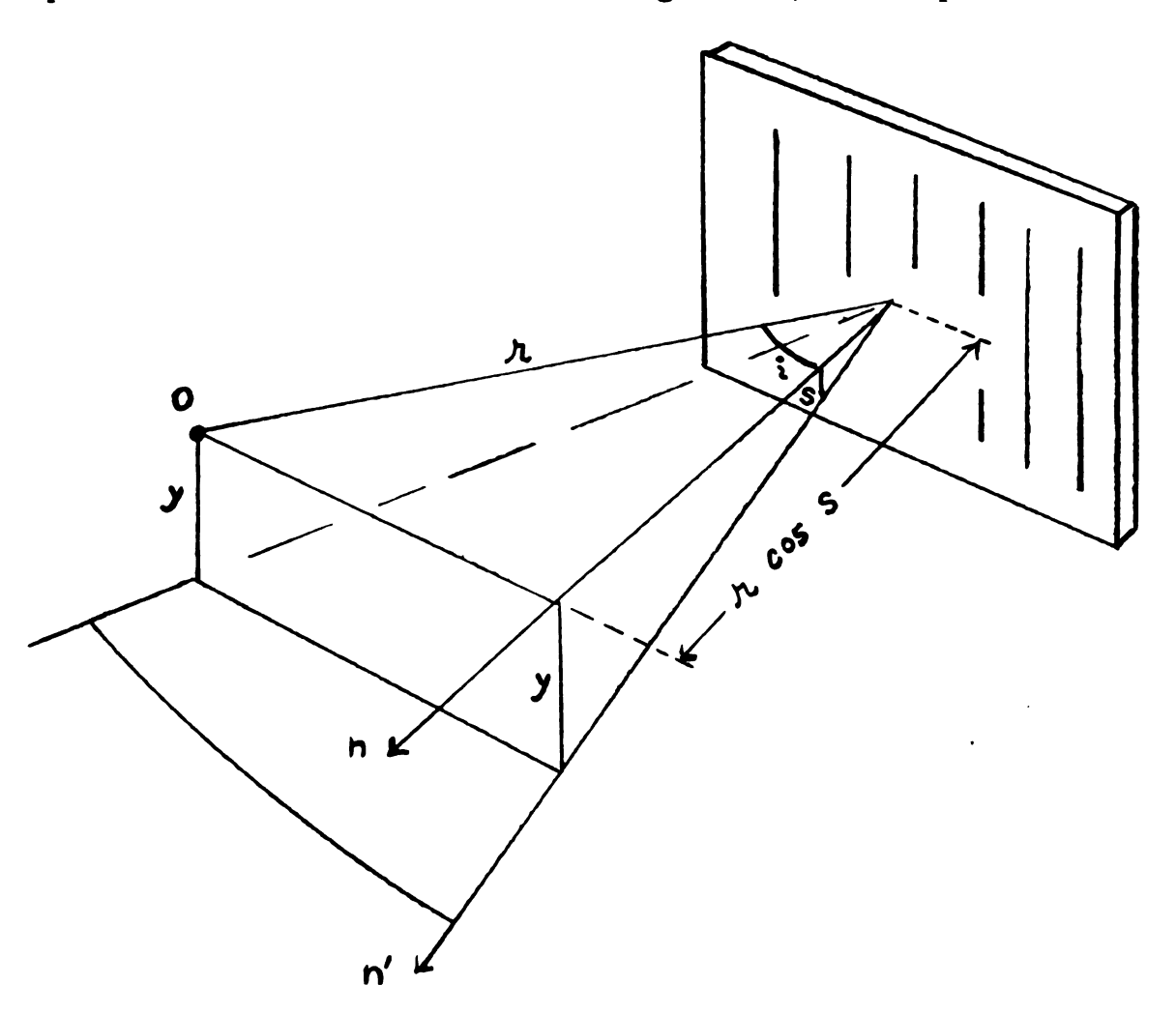


Figure 15. Position of source point 0 with respect to tilted grating.

in a plane which is normal to the grating when properly aligned and which contains the normal n in that position.

The point 0 is a distance y from a similar plane containing the normal \underline{n}' when the grating is tilted through an angle s about an axis perpendicular to the rulings on the grating. For small angles s, sin s and tan s are very nearly equal to s. The distance y may then be represented by y = rs cos i, i being the angle of incidence. A similar expression, involving the angle of diffraction d, gives the distance of the image of 0 from the plane containing \underline{n}' . The displacement D of the image from its position under perfect alignment is then given by

D = rs (cos i + cos d).

This accounts for the shape of curve I in Figure 14. Were no other errors present, the maximum displacement would occur at central image as may be easily verified mathematically.

A rotation of the grating about its normal by an angle R has no effect upon the position of the central image. Such a twist, however, rotates the plane of the spectrum about the reflected beam by the same angle R (3). It is such a displacement that explains the asymmetry of the curves in Figure 14 about the central image position.

The third possible error, i.e. the axis of rotation of the grating not perpendicular to the plane of the axes of the paraboloids, produces no variation in image position at the exit slit. Unless the axis of rotation is normal to the plane of the axes of the paraboloids, the image will be displaced by a fixed distance from its position under perfect alignment.

Were this the only result, there would be no cause for concern. If the axis of rotation is tilted, however, diffracted rays are not parallel to the axis of the paraboloid and aberrations (e.g. astigmatism) are introduced. Consequently, it is desirable that the axes of the paraboloids lie in the plane defined by the motion of the grating normal.

Successive small adjustments were made until the image emerged at a fixed position at the exit slit (sample curves II, III, IV, and V, Figure 13). This condition indicated that the rulings on the diffracting surface were parallel to the axis of rotation. Since the grating axis determines the plane of the system, the operational centers of the slits had to be redefined. Following the procedure previously described, and utilizing the newly defined centers of the slits, the diagonal slit and mirror units of the monochromator were then realigned.

Curvature of Image

Only one point on the slit can be exactly at the focal point of the paraboloid. However, the length of the entrance slit illuminated in practice is small, less than one centimeter, and astigmatism was not measurable with the traveling microscope. On the other hand, upon rotation of the grating through large angles from central image position, one observes significant curvature of the image if the entire entrance slit

is illuminated. This effect results from the fact that a ray originating at a distance from the axis of the paraboloid encounters an effective grating space different from that encountered by an axial ray. According to Randall and Firestone, the resulting image is parabolic if the entrance slit is straight (4).

Image curvature increases as the grating is rotated through greater angles from central image position, and the sense of curvature depends upon the direction of rotation from central image position. The latter fact precludes the use of curved slits because one desires to work with the grating rotated in both directions from central image position (Cf. discussion on page 11). Since the slits are straight, resolving power is reduced if a curved section of the image is utilized, for the exit slit then selects a "chord" from the curved spectrum. In an effort to obtain maximum possible resolution, a segment of the image centered at the center of symmetry of the parabolic image was selected and the entrance slit was accordingly limited to about 8 mm.

Having limited the entrance slit to an arbitrary length, the length of the image of the mercury green line in various orders was measured. Within the accuracy of measurement (\$\frac{1}{2}\$ 0.03 mm), the lengths of slit and images were equal, indicating the absence of astigmatism with paraboloids as adjusted. Thus, the usable portion of the entrance slit

has the same length as the "straight" image segment obtainable. In practice, the length of entrance slit illuminated was less than 8 mm. The signal was about 6 mm in length.

Width of Image

In a spectrum formed by a grating, the grating space determines the dispersion. The width of spectral lines, however, is independent of the grating space. It is determined by the width of the grating and the angles of incidence and diffraction (5). For an infinitely narrow entrance slit, the spectral line is a diffraction pattern, with the grating acting as the diffracting aperture.

Consider an aperture (grating) of width W. For an infinitely narrow monochromatic line source, the central maximum of the pattern formed by the aperture has the half-width f/W, f being the focal length of the focussing lens or mirror and λ the wavelength of the radiation. Even with an infinitely narrow entrance slit, then, there will be considerable overlapping if the source emits radiation of a wide wavelength range. In practice, one must employ slits of finite width. The width of the diffraction maximum is thereby increased. Van Cittert (6) found, however, that, for a source slit illuminated by non-coherent radiation, there is a very slow increase in image width for slit widths up to f/W. He and Schuster (7) agree that such a slit width is

optimum with respect to intensity and width of image. For the apparatus employed, $f\lambda/W = 8$ microns at a wavelength of 1.6 microns.

The full width of the grating is never presented to both the entrance and exit slits, and rarely to either. I.e. In general, the angle in a horizontal plane subtended by the grating at either slit is not a maximum. grating normal should pass through one slit, in which case the angle subtended at that slit is a maximum, the angle subtended at the other slit is certainly less than maximum. The image width, then, is only approximated by the expression $f \mathcal{N} W$. Rather, it is a function of the position of the grating. An expression for the ratio of image width to slit width for relatively wide slits has been derived (8). such conditions (i.e. wide slits), diffraction by the grating is a small effect. In terms of the angle R of rotation of the grating from central image position, this ratio is represented by cos(10.5 - R)/cos(10.5 + R), the angle 10.5 degrees being a constant for the spectrometer. Specifically, it is one half the angle between rays incident upon and reflected from the grating when in central image position.

To verify this expression, the entrance slit of known width was illuminated by a low pressure mercury 198 arc in electrodeless discharge and the width of the image of the ${\rm H_g}^{198}$ green line in various orders for several different

slit widths was measured with the traveling microscope.

Results are indicated in the following table and graphically in Figure 16. Although the observed behavior does not agree

Table I. Ratio, image width/central image width for various entrance slit widths.

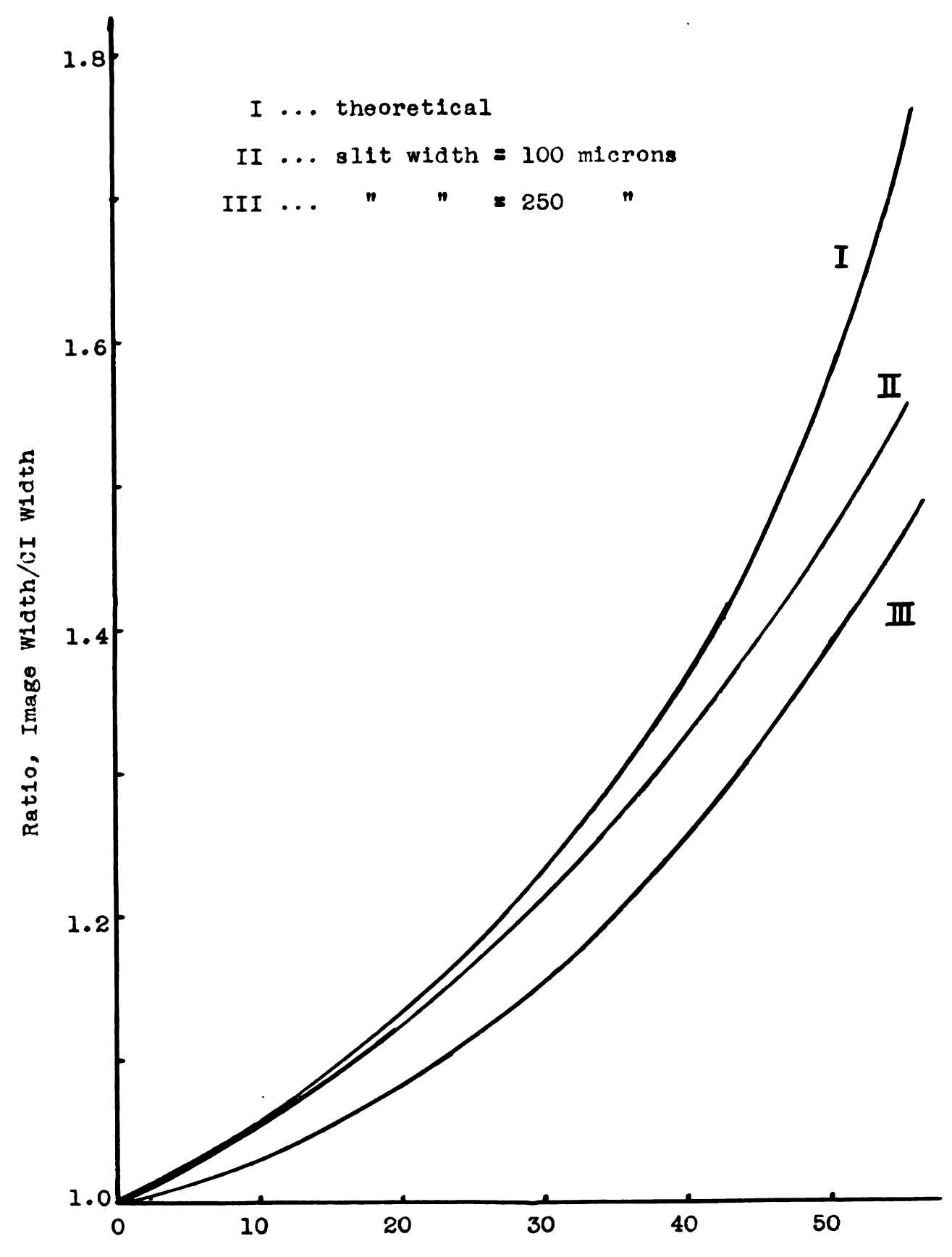
Grating position	50	75	100	200	250	Theor- etical
9.54 deg.	1.027	1.060	1.026	1.051	1.058	1.064
19.34	1.035	1.151	1.078	1.101	1.124	1.127
29.82	1.168	1.253	1.147	1.184	1.213	1.238
41.48	1.274	1.325	1.293	1.272	1.329	1.390
55.95	1.407	1.482	1.474	1.475	1.550	1.759

exactly with that of the theoretical expression, these figures indicate the predicted increase of image width as the grating is rotated farther from central image position. As might be expected, there is better agreement for greater slit width.

Examination of the expression representing the ratio of image width to slit width leads to the observation that, for rotation in the opposite direction (R negative), the ratio decreases as R becomes more negative. This was also observed, and the reciprocal of the above ratio exhibited the same behavior as the ratio itself for positive R.

These observations indicate that, for best results, the instrument should, in general, be operated with entrance slit and exit slit of different widths. As the grating is rotated

·



Grating Position (degrees rotation from CI)

Figure 16. Image width/central image width vs.
rotation of grating from central image.

farther from central image position, the ratio of the slit widths should be adjusted in accordance with the above expression.

Grating Ghosts

During alignment of the 600 line/mm grating, satelites were observed in the neighborhood of the principal image of the mercury green line in various orders. Being near the principal image, and located symmetrically on each side of it, they were probably Rowland ghosts, those produced by periodic errors in the ruling of the grating. In the orders in which the mercury green line was most intense, three of these ghosts were readily visible. Since the grating was certified to produce ghosts of intensity less than 0.05% of that of the parent line in the first order, the intensities of the ghosts were investigated.

Intensities of the ghosts in the third order were measured, utilizing an Aminco microphotometer with the output fed into a Brown recorder. The most prominent ghost had an intensity relative to the parent line of not more than 1.08%. Intensity relative to the parent line increases with the square of the order of the parent line (9 and 5). Consequently, ghosts in the first order near infrared would have a maximum possible intensity of 0.12% and should cause no difficulties in absorption spectra.

Similar tests were not performed for the 400 line/mm grating which was installed at a later date. However, it was certified to produce ghosts of intensity less than 0.07% of that of the parent line in first order.

Amplifiers and Recorder

The signals incident upon the PbS cell and the photomultiplier are amplified and rectified by phase sensitive narrow band amplifiers, and are recorded by a Leeds & Northrup two pen recorder. On a single chart, then, one obtains a record of the infrared signal and a trace representing the variation of intensity of a small portion of the interferometric fringe system. These fringes constitute a frequency scale, with a constant frequency difference between maxima. The frequency interval and the calibration is determined from standard emission lines, at least two of which are required. No corrections for the index of refraction of air are necessary since the etalon is within the evacuated tank.

To permit both pens to range over the width of the paper, they are so adjusted that points of each trace made at the same instant in time are separated laterally by about one eighth of an inch. This displacement must be considered as a second order effect when assigning frequencies to spectral lines.

Absorption Cell

Absorption cells are placed in the auxillary tank, which is connected directly to the primary tank. The tubular connection between the tanks permits the evacuation of both by a single pump and serves as well as an avenue into the spectrometer for the infrared beam. Fused quartz windows in the side and end of the quaillary tank permit use of either a straight or a multiple traverse cell. Suitable outlets and stopcocks permit the introduction of the sample and changes of pressure within the cell while the tank is evacuated and the spectrometer in operation.

The multiple traverse cell employed is of the J. U. White type (2). This particular version incorporates an eight inch pyrex tube as the cylindrical portion of the cell wall and is so designed that adjustments may be made without opening the cell.

Light Sources

As infrared sources, 100 watt and 300 watt zirconium concentrated arc lamps by Sylvania were available. These lamps contain argon as a carrier gas, and lines in the emission spectrum of argon were used for standardization and calibration purposes. A 100 watt zirconium arc lamp was employed as the source for the interferometer system.

SYMMETRIC TOP THEORY

The methyl chloride molecule is axially symmetric, with the chlorine atom situated on the three-fold axis of symmetry of the methyl group and lying outside the pyramid formed by

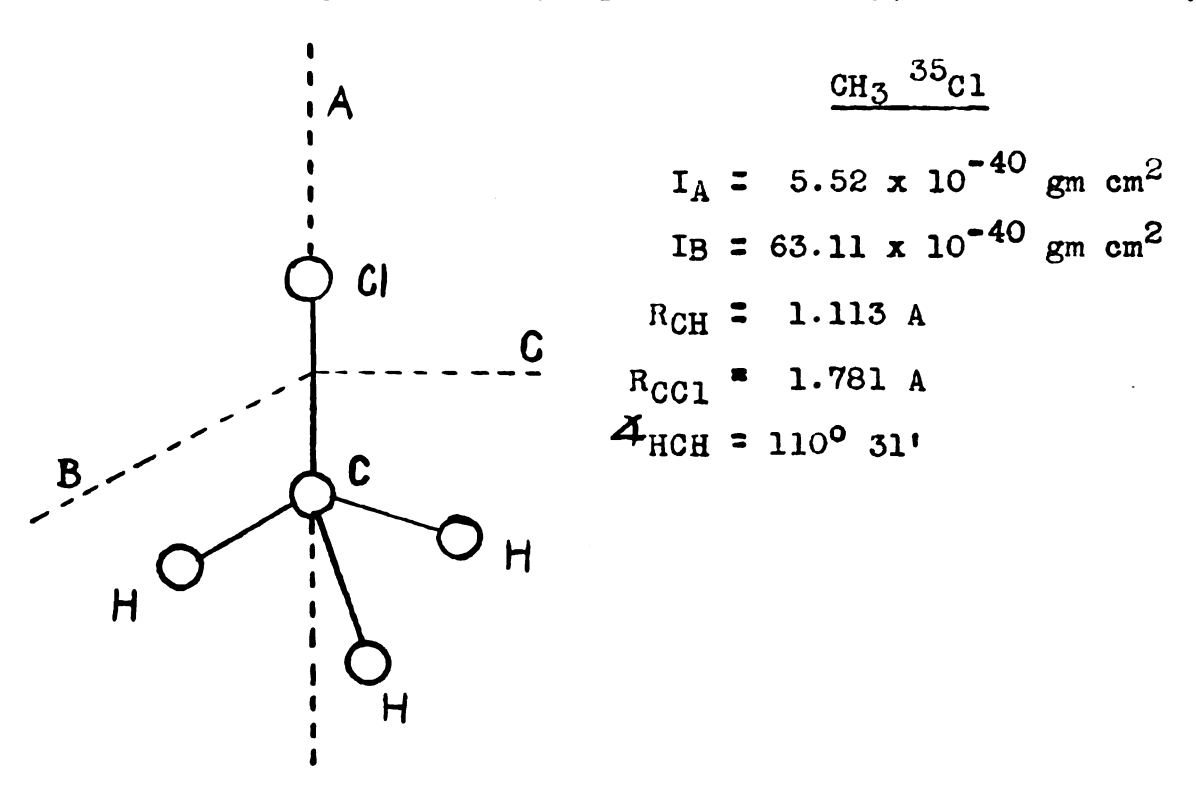


Figure 17. Methyl chloride, showing principal axes, with moments of inertia about the principal axes, and bond lengths and angles. (10 and 11)

the carbon and three hydrogen atoms (Figure 17). A pentatomic molecule, methyl chloride has nine internal degrees of freedom. There are, however, only six normal modes of vibration, three of which are doubly degenerate (Figure 18). These vibrational modes may be labeled according to the principal change in

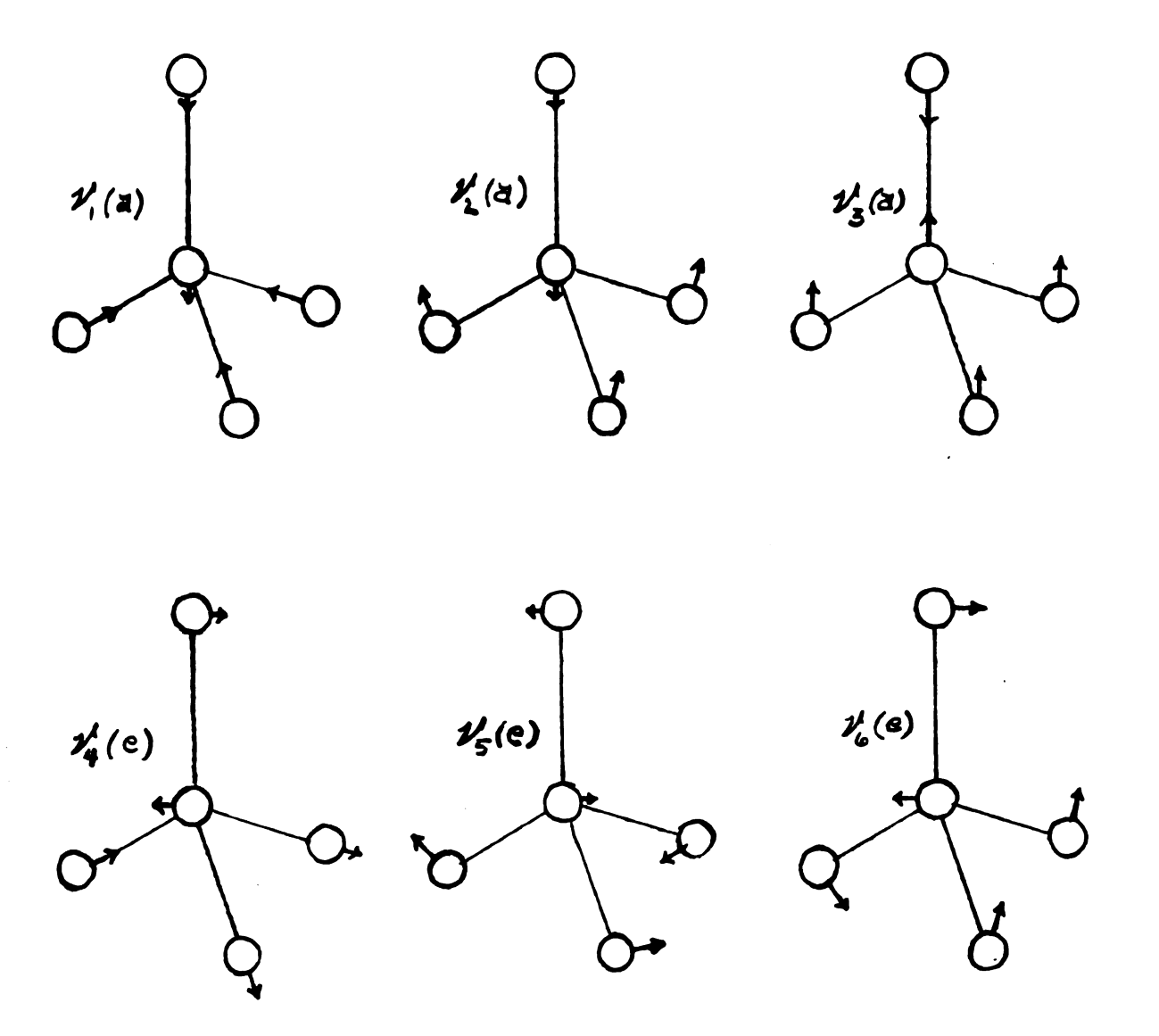


Figure 18. Approximate normal vibrations of CH3Cl. Notation is that of Herzberg. The degenerate modes are denoted by (e).

structure occurring during the motion. In Table II are listed structural variations characteristic of the vibrations along with the different notational assignments used by Herzberg (12) and Dennison (13) respectively.

It is apparent from Figure 18 that the non-degenerate vibrations (a) are axially symmetric. The change of electric dipole moment occurring during these vibrations, then, is parallel to the figure axis. Absorption bands characteristic of transitions from the ground state to these vibrational

Table II. Vibrational Modes in CH3Cl

Herzberg		Dennison
$\mathcal{V}_{1}(a)$	Symmetric C-H stretching	$\mathcal{V}_{\mathtt{l}}$
$\mathcal{V}_{2}^{(a)}$	Symmetric CH3 deformation	2 / ₅
V ₃ (a)	C-Cl stretching	$ u_3$
% _4(e)	Asymmetric C-H stretching	\mathcal{V}_2
ν ₅ (e)	Asymmetric CH3 deformation	\mathcal{V}_4
1 / ₆ (e)	CH ₃ -Cl rocking	ν_{e}

states are called parallel bands. The degenerate vibrations give rise to a change of electric moment normal to the figure axis. So-called perpendicular bands characterize these vibrations.

Vibration-Rotation Energy

The energy of a vibrating rotor may be approximated as the sum of electronic vibrational, rotational, and interaction terms.

T = T(electronic) + T(vibr) + T(rot) + T(interaction)

Since electronic transitions involve energies associated with the ultra-violet, it is assumed for work in the infra-red that the electronic configuration remains unchanged.

Consequently, only vibrational and rotational energies, and any interactions, need be considered.

It is known that for molecules with doubly degenerate vibrations, the vibrational contribution to the term value may be written as in Herzberg (12),

$$G(v) = \sum_{i} w_{i}(v_{i} + \frac{1}{2}d_{i}) + \sum_{i} \sum_{k \geq i} x_{ik}(v_{i} + \frac{1}{2}d_{i})(v_{k} + \frac{1}{2}d_{k}) + \sum_{i} \sum_{k \geq i} g_{ik}l_{i}l_{k}$$
(1)

in which the symbols have the following meanings:

wi ... Classical frequency of ith normal mode.

xik .. Anharmonicity constant.

g_{ik} .. Small constant of approximately the same magnitude as the x_{ik}; g_{ik} = 0 for non-degenerate vibrations.

v₁ ··· Vibrational quantum number of i th normal mode.

 d_1 ... Degeneracy of 1th vibrational mode. $d_1 = d_2 = d_3 = 1$ and $d_4 = d_5 = d_6 = 2$ for CH_3C1 .

 l_1 ... A quantum number assuming the values $l_i = v_i$, $v_i - 2$, ... 1 or 0 for degenerate vibrations, and $l_i = 0$ for non-degenerate vibrations.

For the ground state, all $v_1 = 0$. Consequently, a term involving g_{1k} does not appear in the expression for the ground state energy since all $l_1 = v_1 = 0$.

•
25
4
X
:
<u>:</u>
;
:
:
:
:

Attention will henceforth be focussed upon the vibrational state $2V_4$ (i.e. $v_4 = 2$; all other $v_1 = 0$), which is the excited vibrational level involved in the transition represented by the band examined in this work. For this excited state, the energy expression contains the term g4412. Since the ground state contains no term in gik, the expression for the energy difference corresponding to the transition from the ground state to the state 21/4 also contains the term $g_{44}l_4^2$. This expression has not one value, but two, for 1_4 may assume the values $1_4 = 2$ and $1_4 = 0$. This represents the fact that the state 21/4 has two distinct sub-levels. Consequently, the spectrum resulting from this transition has two components. A parallel band results from the transition to the sub-state $l_4 = 0$ and a perpendicular band results from the transition involving the sub-state 1_4 = 2 (14). That this should be the case may be seen from examination of the wave function. The wave function given by Herzberg (12) contains a factor $exp(\pm i10)$. For 1 = 0, this is a single function and there is no degeneracy. For each value of 1 \$\notine\$0, however, it represents two functions. But the energy depends on 12 for this state. Hence there is a two-fold degeneracy for 14 = 2. Parallel bands result from transitions to non-degenerate states and perpendicular bands from transitions to degenerate states.

The above discussion indicates that the origins of the two components should be separated by $4g_{44}$. Obviously, the constant g_{44} would be known immediately if the origins of both bands could be determined. It was initially proposed to analyze both the parallel and perpendicular components of the band $2\nu_4$. To date, however, it has not been possible to determine the origin of the perpendicular band, for the positions of some of the lines deviate from theory and indicate the presence of a perturbation. Consequently, the constant g_{44} cannot be determined at present. Attention will henceforth be confined to the parallel component only.

For a symmetric top, the rotational energy levels are represented in wave numbers by

$$F(J,K) = BJ(J + 1) + (A - B)K^{2} - D_{J}J^{2}(J + 1)^{2} - D_{JK}J(J + 1)K^{2} - D_{K}K^{4}.$$
 (2)

In this relation, $A = h/8\pi^2 cI_A$ and $B = h/8\pi^2 cI_B$, h being Planck's constant. I_A and I_B are the moments of inertia about the principal axes, with A denoting the unique (figure) axis. The moments of inertia, and consequently the rotational constants A and B, depend slightly upon the state of vibration. The other symbols have the following meanings:

J ... Total angular momentum quantum number.

K ... Quantum number for the component of total angular momentum along the symmetry axis. Obviously, K ≤ J.

 $[\]textbf{D}_{J},~\textbf{D}_{JK},~\textbf{D}_{K}~\dots$ Centrifugal distortion constants.

In some cases, it is possible to disregard effects of centrifugal distortion since the D's are small. To obtain satisfactory results, however, it was found necessary to consider the terms in $D_{\rm J}$, $D_{\rm JK}$, and $D_{\rm K}$.

While centrifugal distortion effects may sometimes be neglected, the interaction of vibration and rotation cannot be disregarded. This Coriolis effect, coupling the components of a degenerate vibrational mode and producing an internal component of angular momentum, necessitates an additional term in the expression representing the energy levels of a vibrating rotor. Called the Coriolis coupling term, it is written $-2AK\sum_{i}(\pm \sum_{i}l_{i})$, in which \sum_{i} is the constant (quantum number) for vibrational angular momentum. In general, \sum_{i} is not an integer, but ranges between zero and unity. The sign of the term depends on whether the component of total angular momentum along the symmetry axis and the vibrational angular momentum are parallel or anti-parallel. For non-degenerate vibrations, \sum_{i} = 0.

Except for the electronic energy which is presumed to remain constant in all transitions considered, the energy levels of a vibrating symmetric top may thus be written

$$T = G(v) + BJ(J + 1) + (A - B)K^{2} - D_{J}J^{2}(J + 1)^{2} - D_{JK}J(J + 1)K^{2} - D_{K}K^{4} - 2AK \sum_{i} (\pm \hat{J}_{1}1_{1}).$$
 (3)

As discussed previously, $G(\mathbf{v})$ assumes two distinct values for the state $\mathbf{v_4} = 2$ (page 35).

Observable transitions from one rotational state to another are governed by clearly defined selection rules. For K the selection rule is $\Delta K = 0$, ± 1 with parallel bands resulting when $\Delta K = 0$, and perpendicular bands when $\Delta K = \pm 1$. Similarly, transitions $\Delta J = 0$, ± 1 may occur, subject to the restrictions that $\Delta J \neq 0$ for K = 0 and for J = 0. Rules governing the changes in the l_1 are more complex. In the case of interest, the lower state (ground state) is non-degenerate while the upper state ($2\nu_4$) is degenerate and has sub-levels corresponding to the possible values of l_1 . It has been stated that a parallel band ($\Delta K = 0$) results from transitions to the rotational levels of the vibrational sub-state $l_4 \equiv 0$. Consequently, Δl_4 is zero and there is no first order Coriolis contribution to the energy in the parallel band (equation 3).

Transition Energies

Before considering the various possible transitions and calculating the expressions for transition energies, the notation to be employed will be set forth. Spectral lines will be designated by principal symbols P,Q, and R corresponding to transitions $\Delta J = -1$, $\Delta J = 0$, and $\Delta J = +1$ respectively. In addition, a left superscript and a right subscript will be used. The superscript P, Q, or R will represent transitions $\Delta K = -1$, $\Delta K = 0$, or $\Delta K = +1$, while

the subscript will denote the value of K for the lower state. E.g. P_{Q_2} designates the transition for which $\Delta J = 0$, $\Delta K = -1$, and K = 2 in the lower state.

By application of the selection rules outlined above, expressions for the frequencies of the various spectral lines may be obtained. In order to obtain simplified expressions for the transition frequencies, the differences between the DJ, D_{JK} , and D_{K} in the upper and lower states were neglected since these constants are themselves small (of the order of $10^{-6}~\rm cm^{-1}$).

For a parallel band $(\Delta K = 0)$, there are three groups of lines, or branches, for each K.

$$Q_{P_{K}} = V_{o} - 2B'J + (B' - B'')(J^{2} + J)$$

$$+ [(A' - B') - (A'' - B'')] K^{2} + 4D_{J}J^{3} + 2D_{JK}JK^{2}$$
(4)
$$Q_{Q_{K}} = V_{o} + (B' - B'')(J^{2} + J) + [(A' - B'') - (A'' - B'')] K^{2}$$
(5)
$$Q_{R_{K}} = V_{o} + 2B'(J + 1) - (B' - B'')(J^{2} + J)$$

$$+ [(A' - B') - (A'' - B'')] K^{2} - 4D_{J}(J + 1)^{3}$$

$$- 2D_{JK}(J + 1) K^{2}$$
(6)

As is customary, J and K refer to the lower state, while the single prime refers to the upper state and the double prime to the lower state. The constant \mathcal{V}_{\bullet} represents the frequency of the vibrational transition or origin of the parallel band.

Sub-Bands

The rotational fine-structure of a band may be approached through the concept of sub-bands. All lines originating in

transitions from ground state levels with the same value of K constitute a sub-band. In the parallel band, for a given K, there will be lines corresponding to $\Delta J = 0$, $\frac{1}{2}$ 1 for all $J \geq K$. Since K cannot exceed J, there will be an increasing number of missing lines for higher K. Examination of the expressions for the frequencies of the QPK, QK, and QRK lines reveals that in any sub-band, the line spacings depend primarily on the B values since the D's are small. If B' and B" differ by very little, as is often the case, the Q branch will appear as a single line while the spacings of the lines in the P and R branches will be approximately 2B' (equations 4 and 6). Whereas B' and B" determine line spacings in each sub-band, the relative positions of the sub-bands depend on (A'- B')-(A"- B"). Typical sub-bands are drawn in Figure 19. If (A'- B')-(A"- B") is large enough to produce a significant shift of the sub-bands the P and R branches may form a confused background on which the Q branches will be prominent separated peaks. If (A'- B') - $(A^n - B^n)$ is such that the sub-bands are displaced relative to each other, and still distinct lines appear in the P and R branches, these "lines" in general represent transitions involving more than one J value.

Intensity Alternation

For molecules of this type, there is an intensity alternation in the spectra arising from the fact that those levels

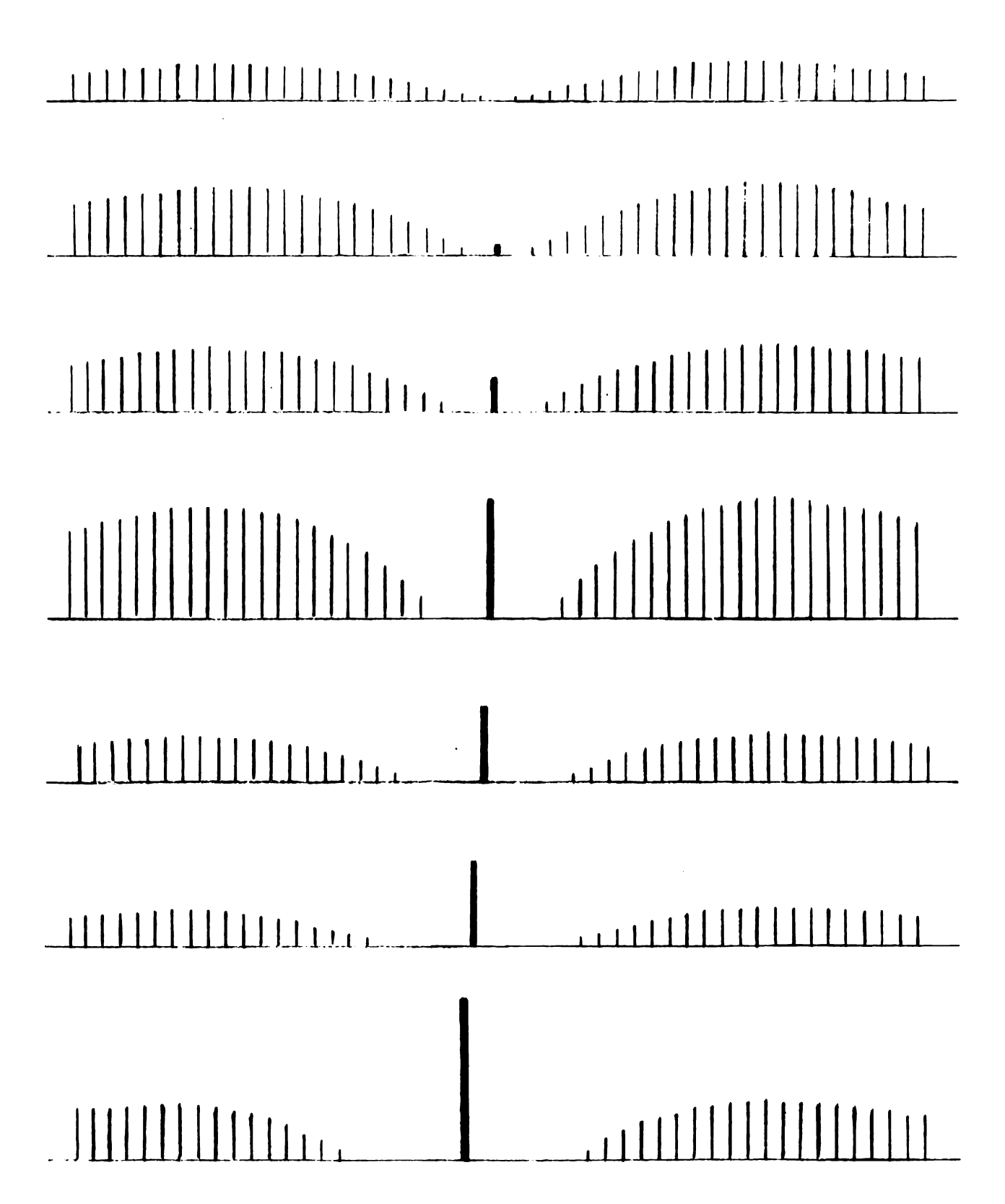


Figure 19. Sub-bands of parallel component of $2 \nu_4$ for K = 0 to K = 6. Intensities of Q branches are drawn to 1/3 scale of P and R lines.

for which K = 3n, n = 1, 2, 3, ..., have twice as many spin states as other levels. This intensity alternation is helpful in assigning quantum numbers to the Q branches and can be observed in Figure 21. In addition, the appearance of the P and R branches in the integrated band is also affected through the greater intensity contributions of the K = 3, 6, 9, ... sub-bands.

Isotope Effect

It would also be expected that the spectra of methyl chloride would reflect the existence of isotopes. There exists more than one isotope of each element comprising the CH₃Cl molecule. In chlorine only, however, are more than one isotope present to a significant degree. ³⁷Cl is about one-third as plentiful as ³⁵Cl, so the band due to CH₃³⁷Cl should be one-third as intense as the CH₃³⁵Cl band.

The two bands will generally be very similar. The band origins should be very nearly the same for $2\frac{1}{4}$ since the Cl is not strongly involved in the motion. However, the line spacings, convergence, etc., will be different. The rotational constant B depends inversely on the moment of inertia I_B which is larger for CH_3 Cl. Consequently, line spacing in the P and R branches of the CH_3 Cl band will be less than in the CH_3 Cl band. Under this condition, the separation of lines with the same K and J values in the two

bands will increase with increasing J. It would be expected, then, that the character of the lines in the P and R branches of the observed band would change with distance from the band origin.

SPECTRA AND ANALYSIS

Spectra were obtained using an absorption path length of about 4 meters with sample pressures ranging from 2 to 5 centimeters of mercury. Monochromator slit widths were about 30 microns, with the ratio of exit slit width to entrance slit width adjusted in accordance with the previous discussion (page 25). The parallel band of 24 is shown in Figure 20.

Wavelength Standards

Frequencies were determined relative to a number of argon emission lines which appeared on the records. These lines occurred in the fourth order grating spectrum, but may be regarded as in second order with respect to the infrared. The wavelengths of these lines, corrected to standard air, are published in Harrison's "M.I.T. Wavelength Tables" (15). Harrison's values for argon in the region of interest were founded primarily upon the interferometric measurements of Meggers and Humphreys (16).

Conversion of the wavelengths in air to vacuum wave number was accomplished by use of the "Tabelle der Schwing-ungszahlen" by Kayser (17) who employed the dispersion formula of Meggers and Peters. Edlen (18) has demonstrated the inaccuracy of the formula of Meggers and Peters, and has calculated corrections that may be applied directly to figures

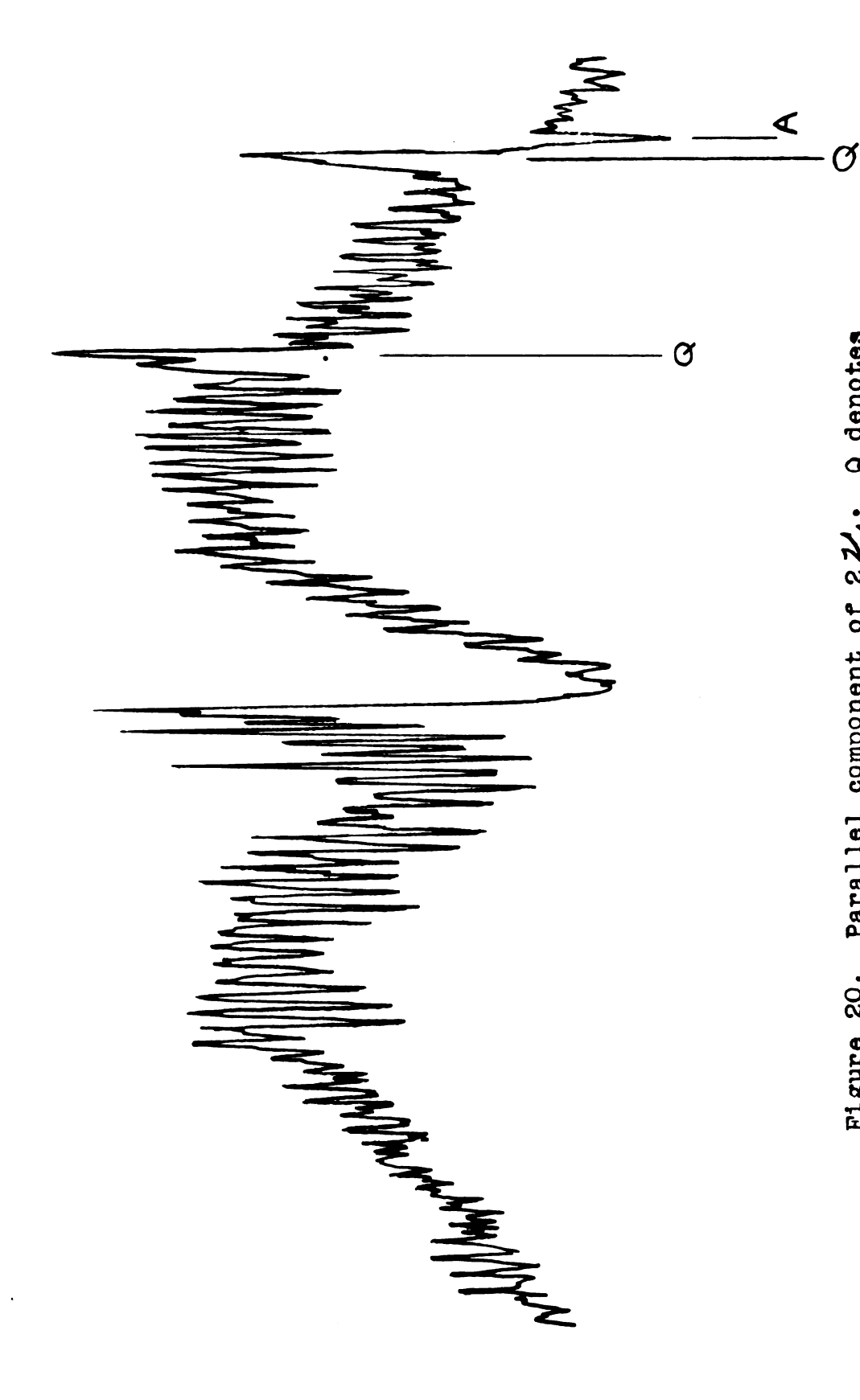


Figure 20. Parallel component of $2 Z_4$. Q denotes Q branches of the overlapping perpendicular component. A denotes an argon emission line.

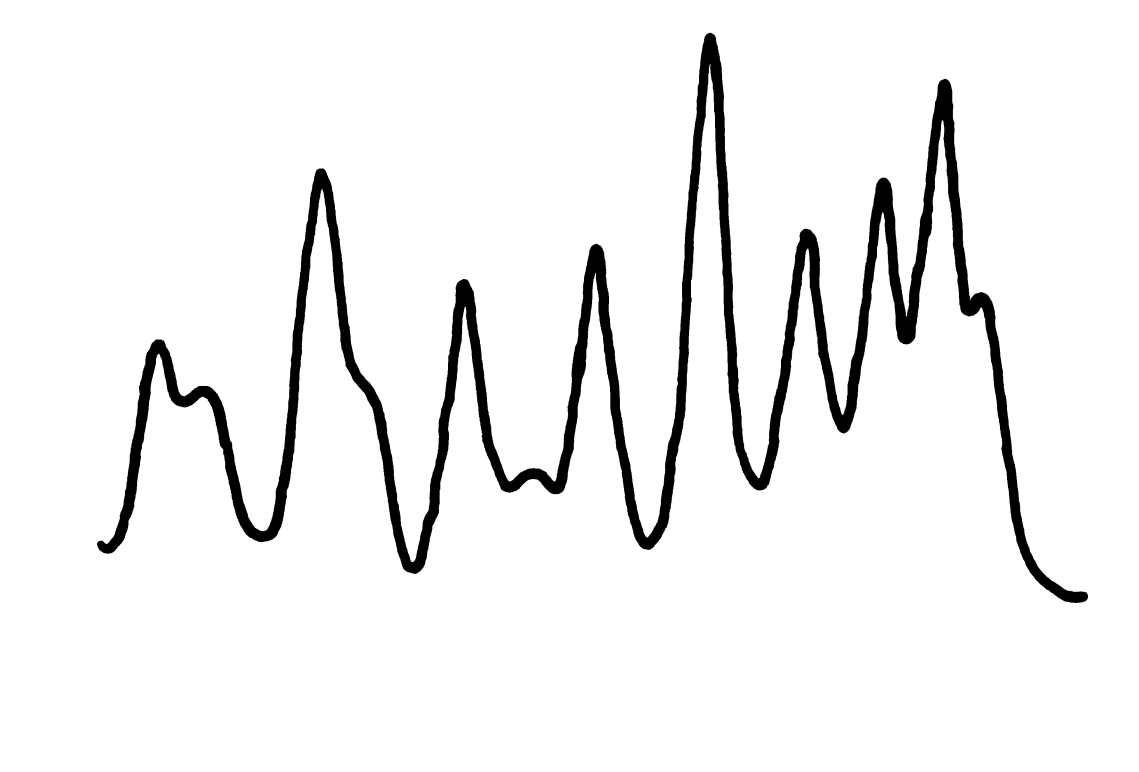
taken from Kayser. These corrections represent the conversion from the dispersion formula of Meggers and Peters to that of Edlen. This correction was applied. Listed in the Table III are the wavelengths in air and relative intensities of the argon lines employed, the vacuum wave number according to Kayser, the Edlen correction, and the vacuum wave number of the standards in second order.

Table III. Argon Emission Lines Used for Calibration

air, Harrison	Relative Intensity	vac, Kayser	Edlen correction	2nd order vac Std.
8006.156A	600	12486.959cm ⁻¹	-0.005cm ⁻¹	6243.477cm ⁻¹
8014.786	800	12473.511	11	6236.753
8103.692	2000	12336.668	11	6168.332
8115.311	5000	12319.003	**	6159.499
8264.521	1000	12096.596	-0.004	6048.296
8408.208	2000	11889.878	*	5944.937
8424.697	2000	11866.676	Ħ	5933.336
8521.441	20 00	11731.883	17	5865.942

Q Branches

By considering the intensity alternation, it was relatively easy to identify the Q branches corresponding to K = 2 to K = 10 (Figure 21). Since the shape of the lines indicated $B^{\bullet}-B^{\bullet}$ to be small, the Q branch frequencies were



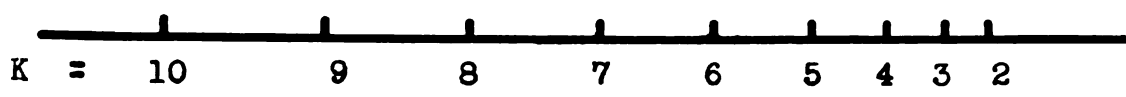
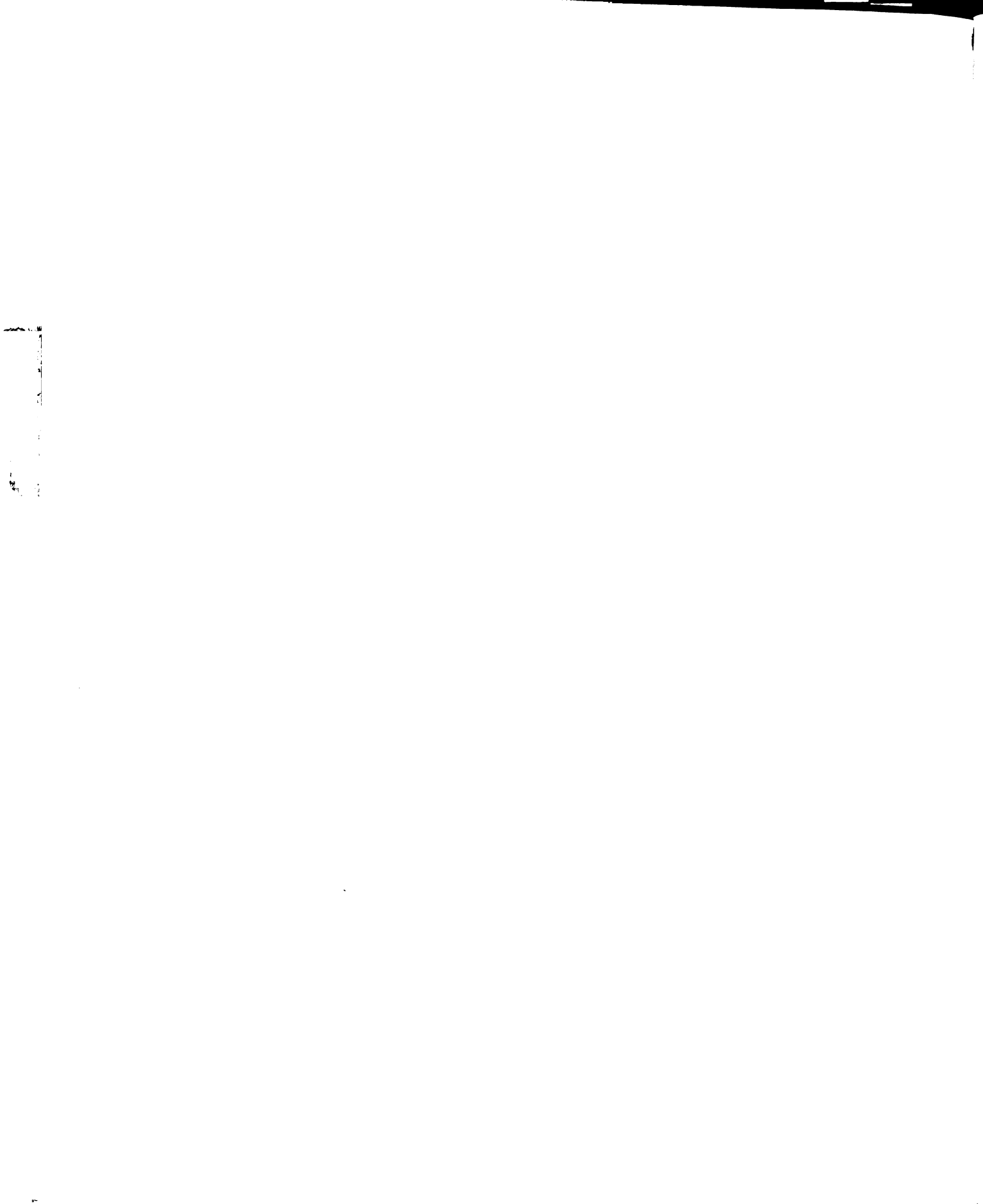


Figure 21. Q branches.



fitted to the formula (from equation 5)

$$\nu = \nu + [(A' - B') - (A'' - B'')] K^2$$
 (7)

A least squares analysis yielded the following results:

$$2'_{0} = 6015.56 \text{ cm}^{-1}$$
(A'- B')-(A"- B") = -0.0481 cm⁻¹

Coserved and calculated for the ${}^Q\!_K$ are listed in Table IV, and the fit is illustrated graphically in Figure 22. In order to expand the ordinate scale in Figure 22, thereby

Table IV. Q Branches

K	V obs	Vcalc	
2	6015.36 cm ⁻¹	.37	+. 01
3	6015.13	.13	.00
4	6014.80	.79	01
5	6014.36	.36	.00
6	6013.82	.83	+. 01
7	6013.20	.20	.00
8	6012.50	. 4 8	C2
9	6011.67	. 66	01
10	6010.75	.75	.00

increasing the accuracy of the determination and making it easier to estimate deviations, a line of slope 0.04 has been added to the experimental data. The quantity (A'-B')-(A"-B") is then -0.04 plus the slope of the resulting line.

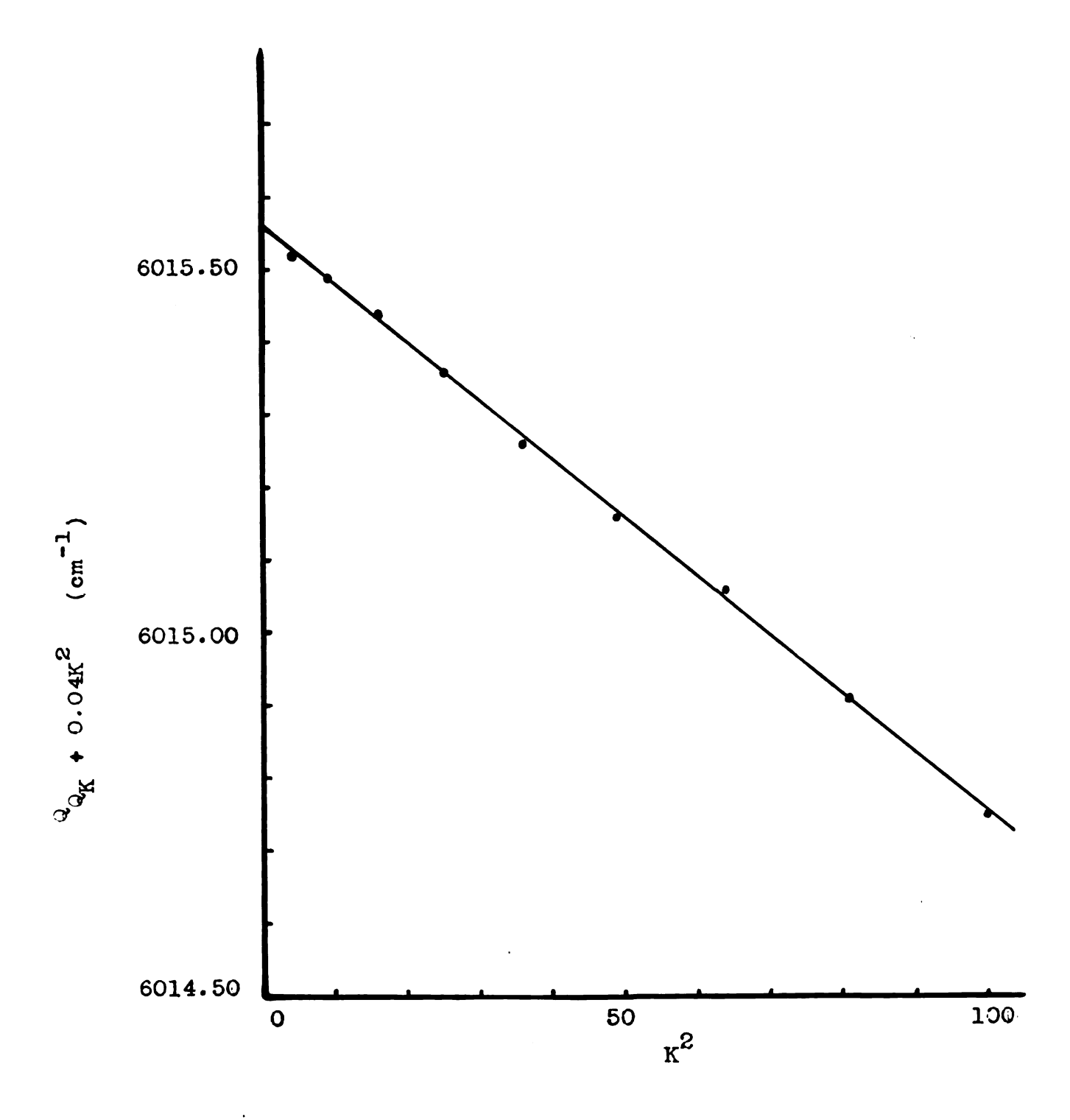


Figure 22. $^{Q}_{Q_{K}} + 0.04K^{2}$ vs K^{2}

Identification of K=3 Sub-band

The positions of the Q branches indicate the manner in which the sub-bands are superposed. Their origins do not coincide, but are displaced from the band origin by an amount depending on K². Consequently, any line which appears in the integrated P and R branches will in general represent several different J values as well as different K values.

Under the highest resolution available with this instrument, it was observed that the P and R branch "lines" in general exhibited a relatively sharp minor peak on the low frequency side of a more intense broad line (Figure 23a). Assuming approximate values for A' and B', and neglecting B'-B" and centrifugal distortion terms, intensities were calculated from formulas given in Herzberg and trial subbands were plotted. Upon displacing the sub-bands relative to each other as required by the measured positions of the Q branches, it was apparent that the minor peak was due primarily to the line in the K = 3 sub-band (Figure 23d). The P and R branch analysis was performed on this series of lines, treating them as components of the K = 3 sub-band.

It was possible to identify a number of lines in the K = 3 sub-band for low J values (5-15) and a number at high J values (20-34). For intermediate J, however, the line

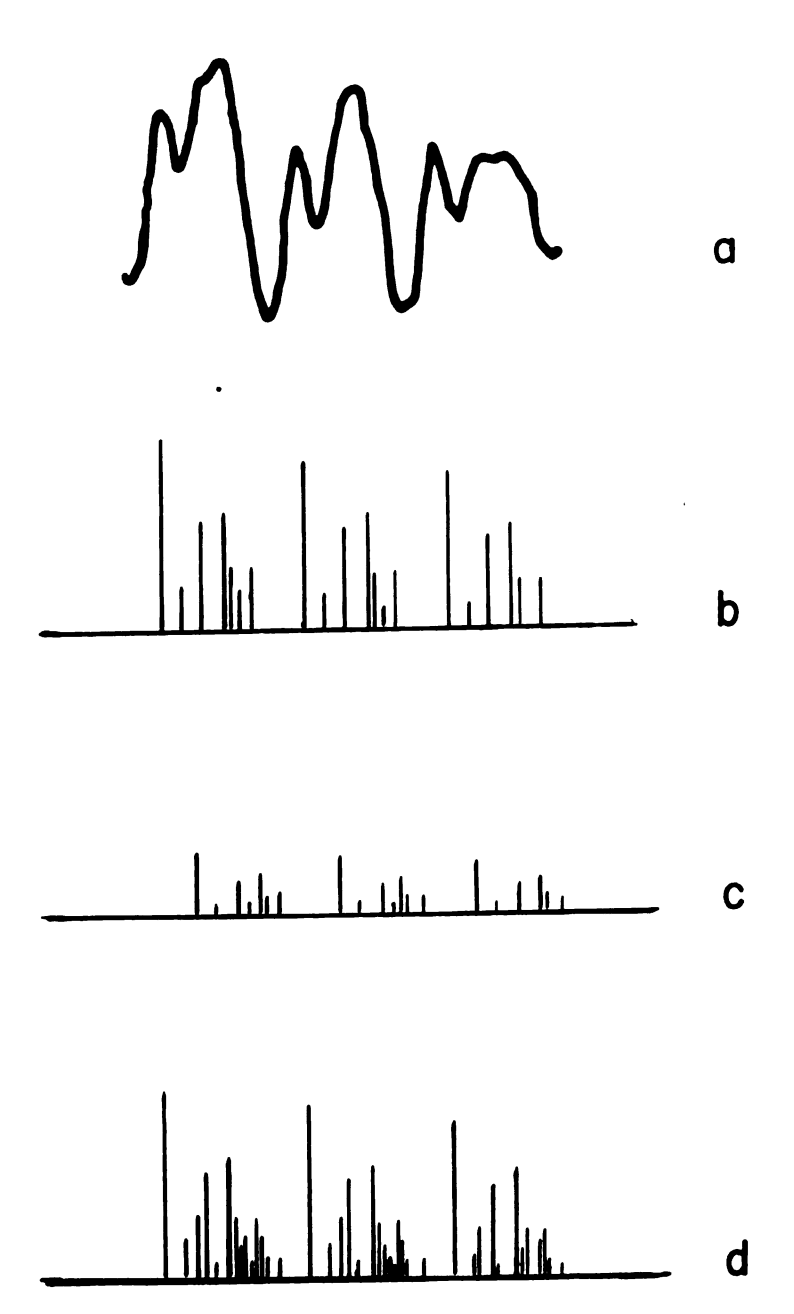


Figure 23. Line structure for P(8), P(9), and P(10). (a) Observed. (b) and (c) Calculated structure for CH3 Cl and CH3 37Cl. (d) Predicted structure.

· ·
;
:
:
:
:
·
·
•
:
:
:

In the R branch, the lines in this region were unusually sharp, while those in the corresponding region in the P branch were broad. In addition, the spacings are also altered. Were these regions omitted, the remaining data would indicate no gross irregularity. Yet, in this region in the R branch, there appears to be one excess line. In the corresponding region in the P branch, there is one line less than expected. It was expected that line shape would change, but due only to the presence of the CH₃³⁷Cl band. The isotope effect, however, could not account for the reduced width of lines in the R branch. A possible explanation will be considered in a subsequent section.

P and R Branch Analysis

In order to determine the rotational constants B^{*} and B^{*} and their difference B^{*} - B^{*} , the method of combination sums and differences was employed. From equations (7) and (9), if K is constant,

$$R(J) - P(J) = 4B'(J + \frac{1}{2}) - 4D_{J}[J^{3} + (J + 1)^{3}]$$

$$- 2D_{JK}(2J + 1)K^{2}$$

$$R(J - 1) - p(J + 1) = 4B''(J + \frac{1}{2}) + 4D_{J}[J^{3} + (J + 1)^{3}]$$

$$+ 2D_{JK}(2J + 1)K^{2}$$
(12)

...

:

•:

$$R(J-1) + P(J) = 2 \frac{\nu}{0} + 2 [(A'-B') - (A''-B'')] K^2 + 2(B'-B'') J^2$$
 (13)

in which the differences between the centrifugal distortion constants in the upper and lower states have been neglected. Since attention is directed exclusively to a particular subband of the parallel band, the superscript and subscript formerly associated with the principal line symbol have been dropped.

Equation (13) is free from terms in D_J and D_{JK} , so the sums R(J-1) + P(J) permit the immediate determination of $B^* - B^*$. The sums were formed and plotted against J^2 (Figure 24). A least squares calculation yielded the values

$$B' - B'' = 0.00044 \text{ cm}^{-1}$$

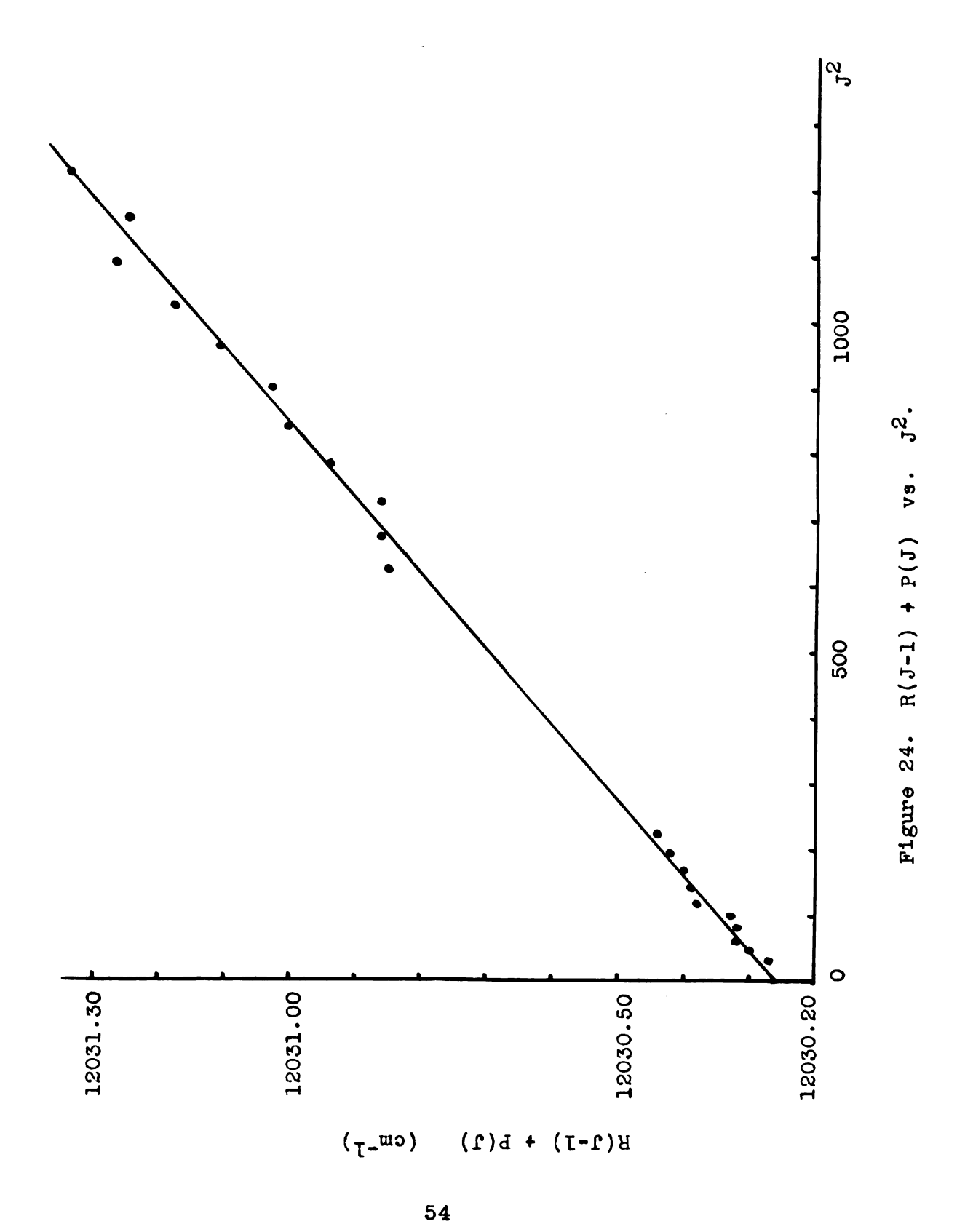
$$\nu_{\rm O}$$
 + $[(A' - B') - (A'' - B'')] K^2 = 6015.13 cm-1.$

The latter quantity is the center $\mathcal{V}_0(\text{sub})$ of the sub-band, and will henceforth be referred to as such. A graphical analysis produced the same value of $\mathcal{V}_0(\text{sub})$, but gave $B^* = B^* = 0.00043 \text{ cm}^{-1}$.

In order to calculate B' and B" from the differences represented by equations (11) and (12), microwave values for D_J and D_{JK} given by Thomas, Cox, & Gordy were assumed (19).

$$D_J = 6.04 \times 10^{-7} \text{ cm}^{-1}$$

 $D_{TK} = 6.60 \times 10^{-6} \text{ cm}^{-1}$



The quantities $4D_J \left[J^3 + (J+1)^3\right]$ and $2D_{JK}(2J+1)K^2$ were calculated. These were then added to the values obtained for R(J) - P(J) and subtracted from R(J-1) - P(J+1). The resulting sets of data were plotted against $4B^*(J+\frac{1}{2})$ and $4B^*(J+\frac{1}{2})$ respectively. The results are shown graphically in Figures 25 and 26 in which a line of slope 1.76 cm⁻¹ has been subtracted. By means of least squares fits, B^* and B^* were calculated to be

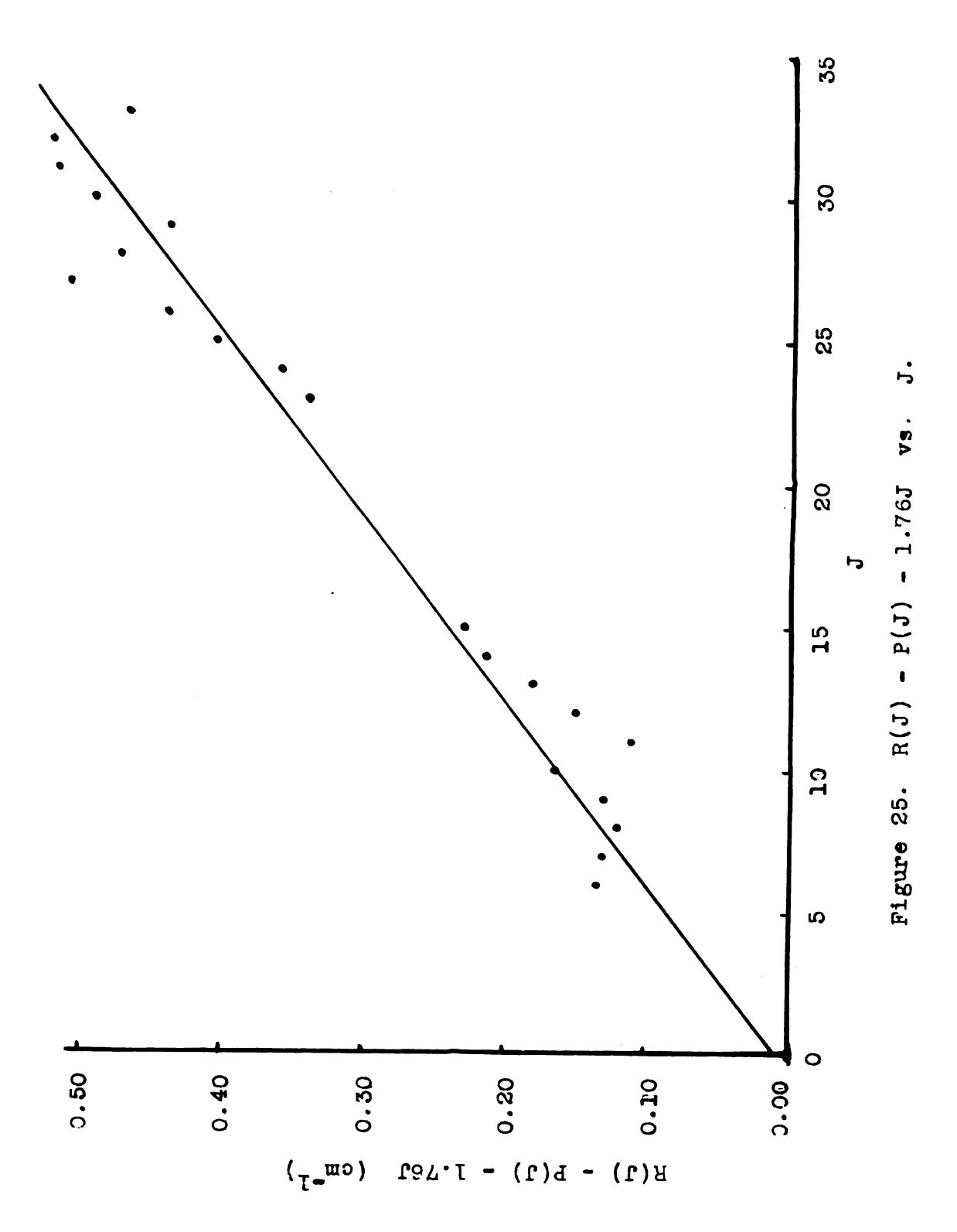
$$B' = 0.4439 \text{ cm}^{-1}$$

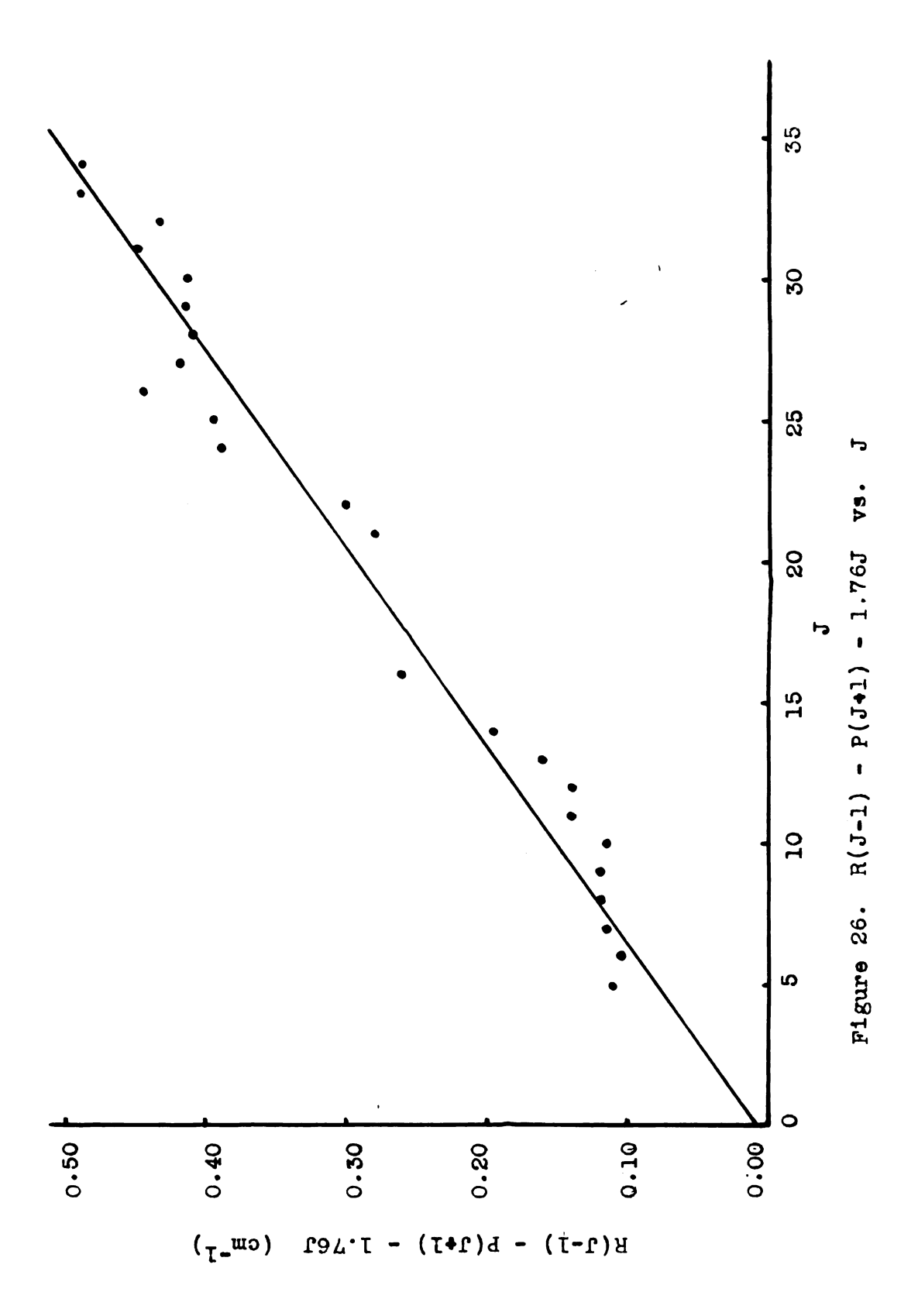
 $B'' = 0.4436 \text{ cm}^{-1}$

Summary of Results

Uncertainties in the values of the constants extracted from the data were calculated by two different methods. In every case, the uncertainty was obtained by the standard method for propagation of errors, beginning with the estimated uncertainties in measured line frequencies. I.e. If F is a function of x_1, x_2, \ldots , and the uncertainty in each x_1 is δx_1 , then the uncertainty δF in F is

In addition, in the two cases in which data was fitted to a function of the form mx + b where m and b are constants,





the probable errors in the constants so determined were calculated from the residuals as set forth by Birge (20).

In order to simplify calculation of the propagated uncertainties, the same uncertainty was assigned to all lines involved in any given calculation. From the range of measured values for the frequency of a given line, the standard deviation for each line was estimated as suggested by Cameron (21). Then, a representative standard deviation was chosen and assigned as the uncertainty in the average measured frequency in all lines. By this method, the uncertainties obtained are 0.03 cm⁻¹ for lines in the P and R branches and 0.02 cm⁻¹ for the Q branches. Utilizing these uncertainties, the propagated uncertainties in the constants were calculated. These are listed in Table V along with the values of the various constants.

Table V. Summary of Constants

Constant	Value in cm ⁻¹	Uncertainty
1 %	6015.56	0.03
(A'- B') - (A'- B')	-0.0481	0.0006
В	0.4439	0.0001
B**	0.4436	0.0001
B' - B"	0.00044	0.00002
2 0(sub)	6015.13	0.02

In view of the excellent fit to the Q branches (Cf page 48), the uncertainties in ν_0 and (A' - B') - (A'' - B'')

appear too large. Utilizing Birge's formulae, the uncertainties in these constants were calculated from the deviations. The results are summarized as follows:

$$2_0 = 6015.56 \pm 0.01 \text{ cm}^{-1}$$
(A'-B') - (A"-B") = -0.0481 ± 0.0001 cm⁻¹

It is felt that these uncertainties are more reasonable than those listed in Table V though they may be too optimistic. Similar calculations for B'-B'' and $\mathcal{V}_{0}(\operatorname{sub})$ yielded errors unreasonably small.

It should be noted that, while the uncertainty in B" is 0.0001 cm⁻¹, the value B" = 0.4436 cm⁻¹ obtained from the data differs from the microwave value B" = 0.4434 cm⁻¹ by 0.0002 cm⁻¹. In other respects, however, there is consistency in the results. The values for B', B", and B'-B" are compatible within the limits of uncertainty. The value $V_0(\text{sub}) = 6015.13 \text{ cm}^{-1}$ obtained from the fit to the sums R(J-1) + P(J) is the same as that calculated for K = 3 from the constants V_0 and (A'-B')-(A''-B'') yielded by the Q branch analysis. Furthermore, there is agreement with the measured frequency of the K = 3 Q branch (6015.13 cm⁻¹).

Utilizing the constants listed in Table V, and D_J and D_{JK} from microwave results, the frequencies of P and R branch lines in the K = 3 sub-band were calculated. These are listed in Tables VI and VII.

From the values obtained for (A'-B')-(A''-B'') and B'-B'', a value for the difference A'-A'' may be calculated. This is found to be A'-A'' = -0.0477 cm⁻¹, with essentially the same uncertainty as in (A'-B')-(A''-B'').

The constants A and B are inversely proportional to I_A and I_B respectively. Since B'-B''>0 and A'-A''<0, I_B is smaller in the upper state than in the ground state, and I_A is larger in the upper state than in the ground state. A possible change in the configuration of the molecule compatible with these changes would be an increase in the HCH angle.

Table VI. P Branch

<u>J</u>	P(J)obs	P(J)calc	Δ
6	6009.30 cm ⁻¹	.82	+.02
7	6008.93	.94	+.01
8	6008.06	•06	.00
9	6007.18	.18	.00
10	6006.30	•30	.00
11	6005.44	• 43	01
12	6004.57	•55	02
13	6003.69	. 67	02
14	6002.90	.80	.00
15	6001.92	.93	+. 01
16			
17	6000.13	.19	+. 06
18			
19			
20			
21			
22	5995 .99	•35	14
23	5995 .07	4.98	09
24	5994.18	.12	06
25	5993 .27	.26	01
26	5992.39	.40	+.01
27	5991.48	.54	+. 06
28	5990.66	.68	+.02

Table VI. continued

J	P(J)obs	P(J)calc	Δ
29	5989.83	•83	•00
30	5988.97	.97	.00
31	5988.11	.12	+.01
32	5987.27	.27	•00
3 3	5986.45	.4 2	03
34	5985.56	. 57	+.01
35	5984.69	.72	+.03

Table VI. continued

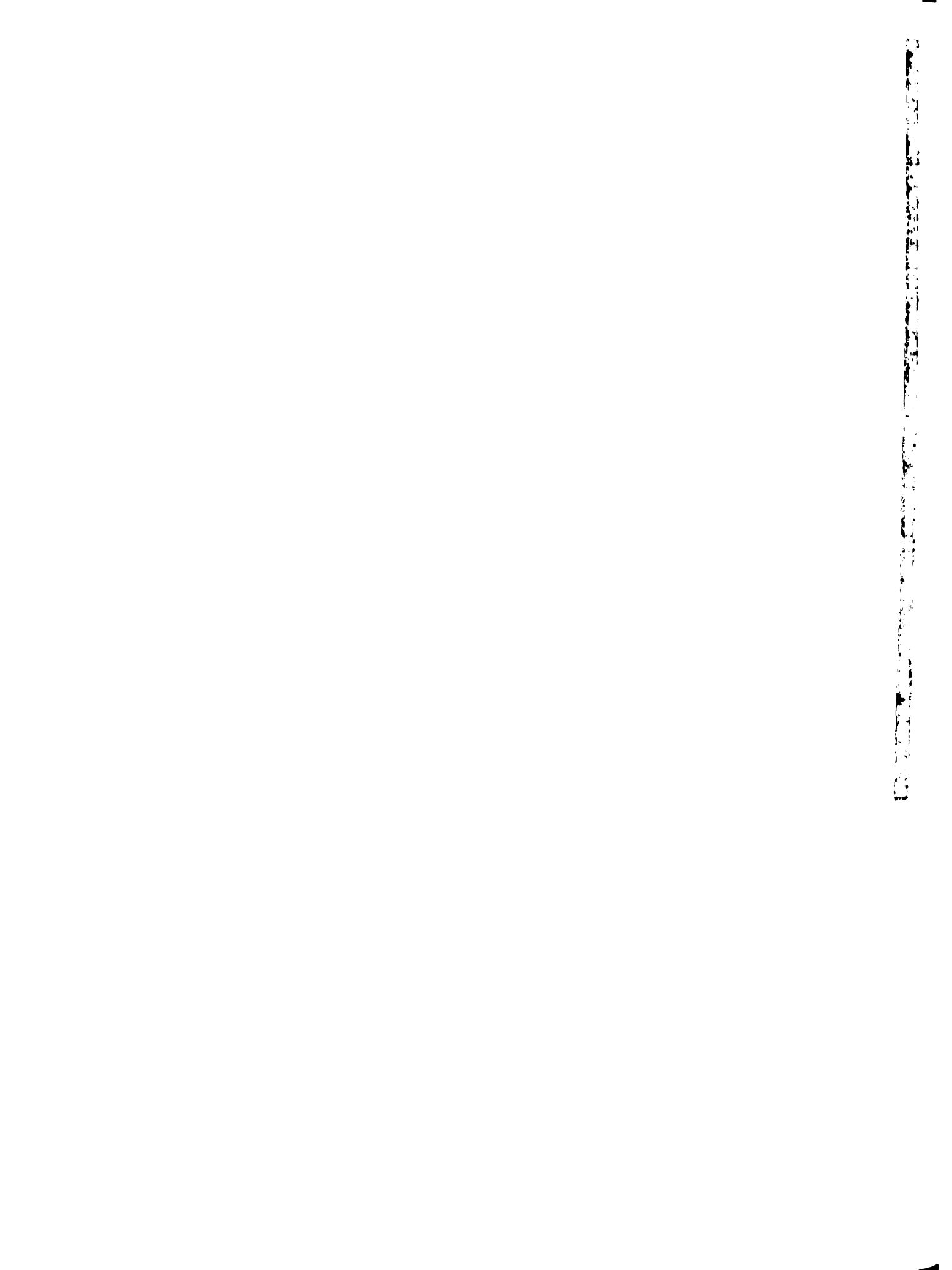
J	P(J)obs	P(J)calc	Δ
29	5989.83	.83	.00
30	5988.97	.97	.00
31	5988.11	.12	+.01
32	5987.27	.27	•00
3 3	5986 .45	.42	03
34	5985.56	. 57	+.01
35	5984.69	.72	+.03

Table VII. R Branch

J	R(J)obs	R(J)calc	Δ
4	6019.59 cm ⁻¹	• 58	01
5	6020.47	. 47	.00
6	6021.37	•36	01
7	6022.26	.26	.00
8	6023.14	.15	+.01
9	6024.03	•05	+.02
10	6024.94	.94	.00
11	602 5.82	.84	+. 02
12	6026.71	.73	+.02
13	6027.62	• 63	+.01
14	6028.52	.53	+.01
15	6029.41	. 43	+. 02
16			
17			
18			
19			
20	603 4. 06	3.94	12
21	6034.91	.84	07
22			
23	6036 .7 0	• 65	05
24	6037.58	.55	03
25	6038.47	.46	01

Table VII. continued

J	R(J)obs	R(J)calc	<u> </u>
26	60 39 . 33	.36	02
27	6040.28	.27	01
23	6041 17	.17	•00
29	6042.06	•08	+.02
30	6043 .0 0	2.99	01
31	6043.91	.90	01
32	6044.82	.90	02
33	6045.69	.71	+.02
34	6046.65	.62	03



Perturbation

Upon examination of Tables VI and VII, it is seen that the agreement between observed and calculated line frequencies is generally good except near the regions for J = 16 to J = 20. For J close to and greater than 20, the deviations are significantly negative. This would be the case were the upper state levels perturbed in the neighborhood of J = 20. If such a perturbation exists, lines about some "center" in each branch would be displaced from the positions predicted by theory. In the R branch, the lines would be displaced in both directions away from the "center". In the P branch, the displacements would be toward the "center". This is indicated in Figure 27.

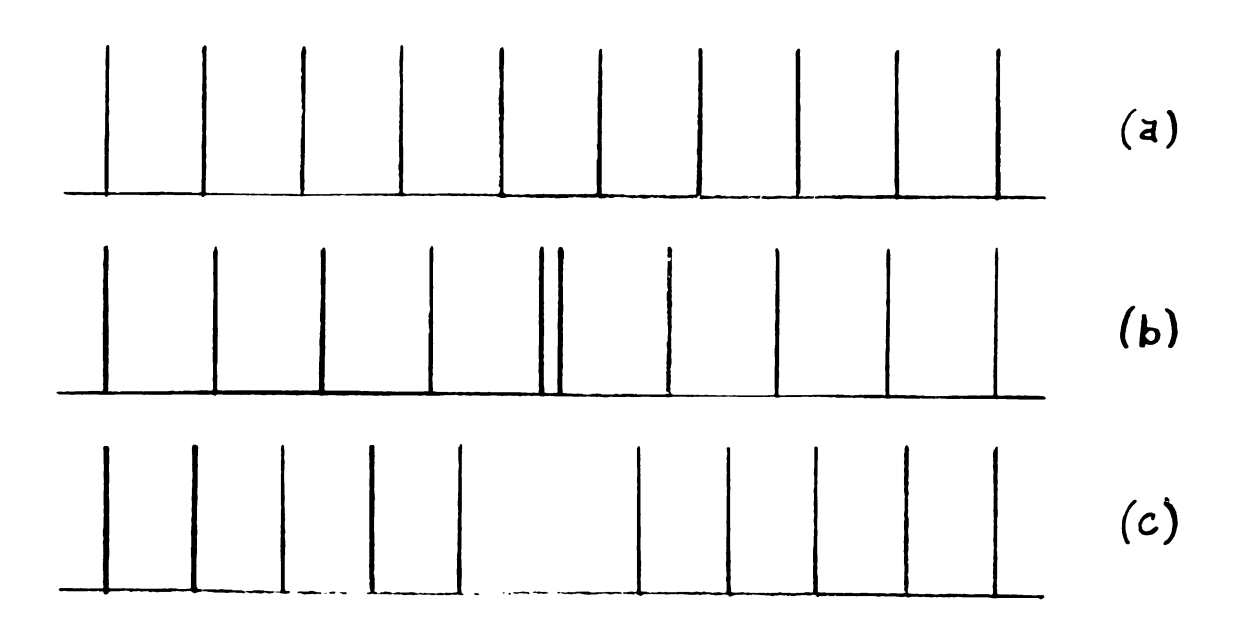


Figure 27. Line shift for perturbed upper state. In absence of a perturbation, line positions are as drawn in (a). (b) and (c) represent P and R branches respectively when upper state is perturbed.

The "extra" line in the R branch and the "missing" line in the P branch could perhaps be explained if lines in the K = 3 sub-band are positioned as in Figure 27, and if other sub-bands are similarly perturbed.

On the high J side of the disturbed region in either branch, calculated line frequencies should be low. Consequently the negative deviations obtained are compatible with the supposition of a perturbation. Similarly, on the low J side of the disturbed regions, the deviations would be positive. For only one line, J = 17 in the P branch, is this observed. As discussed on page 50, other lines between J = 16 and J = 20 could not be identified for measurement. It is entirely possible, then, that the K = 3 sub-band is obscured in the regions J = 16 to J = 20 because of a perturbation.

Note on Isotope Effect

Contrary to expectation, lines in the P and R branches due to $\text{CH}_3^{37}\text{Cl}$ could not be identified as such. Assuming an approximate value for B' for $\text{CH}_3^{37}\text{Cl}$, the shift would be most likely to be observed in the R branch near J = 15 where the line in the K = 3 sub-band for $\text{CH}_3^{37}\text{Cl}$ should fall in the minimum on the low frequency side of the corresponding line for $\text{CH}_3^{35}\text{Cl}$.

There are, however, some indications of absorption by CH₃³⁷Cl. In the region J = 11 to 13 in the R branch, the absorption minima on the low frequency side of lines in the

K = 3 sub-band are not as pronounced as elsewhere in the band. This could be due to the separation of the K = 3 sub-band of $CH_3^{37}Cl$ from that of $CH_3^{35}Cl$. For J = 23 to 34 in the R branch, there is possible evidence of $CH_3^{37}Cl$ absorption on the side of the K = 3 sub-band lines of $CH_3^{35}Cl$. Finally, one might expect the peaks attributed to the K = 3 sub-band of $CH_3^{35}Cl$ to be shifted slightly toward the band origin at low J (10 to 15) due to the presence of the $CH_3^{37}Cl$ band. Tables VI and VII show the deviations for these J values to be generally negative in the P branch and positive in the R branch. These three features are the only apparent manifestations of the isotope effect.

BIBLIOGRAPHY

- 1. R. H. Noble, J. Opt. Soc. Am. 43, 330 (1953)
- 2. N. L. Nichols, Thesis (Michigan State College) (1953)
- 3. R. A. Sawyer, Experimental Spectroscopy, New York: Prentice-Hall (1946)
- 4. H. M. Randall and F. A. Firestone, Rev. Sci. Inst. 9, 404, (1938)
- 5. C. F. Meyer, Diffraction, Ann Arbor: J. W. Edwards (1949)
- 6. P. H. van Cittert, Z. f. Physik 65, 547 (1930)
- 7. A. Schuster, Astrophys. J. 21, 197 (1905)
- 8. T. H. Edwards, Thesis (University of Michigan) (1954)
- 9. J. A. Anderson, J. Opt. Soc. Am. 6, 434 (1922)
- 10. C. H. Townes and A. L. Schawlow, Microwave Spectroscopy, New York: McGraw-Hill (1955)
- 11. Simmons, Gordy, and Smith, Phys. Rev. 74, 243 (1948)
- 12. G. Herzberg, Infrared and Raman Spectra of Polyatomic Molecules, New York: Van Nostrand (1945)
- 13. T. Y. Wu, Vibrational Spectra and Structure of Polyatomic Molecules, Ann Arbor: J. W. Edwards (1946)
- 14. G. Herzberg and L. Herzberg, Can. J. Res. 27B, 332 (1949)
- 15. G. R. Harrison, M.I.T. Wavelength Tables, New York: J. Wiley & Sons (1939)
- W. F. Meggers and C. J. Humphreys, U.S. Nat. Bur. Stds. J. of Res. 13, 293 (1934)
- 17. H. Kayser, Tabelle der Schwingungszahlen, Leipzig: S. Hirzel (1925)
- 18. B. Edlen, J. Opt. Soc. Am. 43, 339 (1953)
- 19. Thomas, Cox, and Gordy, J. Chem. Phys. 22, 1718 (1954)
- 20. R. T. Birge, Phys. Rev. 40, 207 (1932)
- 21. J. M. Cameron, Fundamental Formulas of Physics, Chapter 2, New York: Prentice-Hall (1955)

- 22. T. A. Wiggins, E. R. Shull, and D. H. Rank, J. Chem. Phys. 21, 1368 (1953)
- 23. Miss J. Pickworth and H. W. Thompson, Trans. Far. Soc. 50, 218 (1954)

406.7 6 6 6 6 6 1 1 1 20 1 7

i

!

MICHIGAN STATE UNIVERSITY LIBRARIES

3 1293 03082 1429